

# TWISTED DWARF1 Mediates the Action of Auxin Transport Inhibitors on Actin Cytoskeleton Dynamics

Jinsheng Zhu,<sup>a,1</sup> Aurelien Bailly,<sup>a,b</sup> Marta Zwiewka,<sup>c</sup> Valpuri Sovero,<sup>b</sup> Martin Di Donato,<sup>a</sup> Pei Ge,<sup>a,2</sup> Jacqueline Oehri,<sup>a,d</sup> Bibek Aryal,<sup>a</sup> Pengchao Hao,<sup>a</sup> Miriam Linnert,<sup>e,3</sup> Noelia Inés Burgardt,<sup>e,f</sup> Christian Lücke,<sup>e</sup> Matthias Weiwad,<sup>e,g</sup> Max Michel,<sup>h</sup> Oliver H. Weiergräber,<sup>h</sup> Stephan Pollmann,<sup>i</sup> Elisa Azzarello,<sup>j</sup> Stefano Mancuso,<sup>j</sup> Noel Ferro,<sup>k</sup> Yoichiro Fukao,<sup>l,4</sup> Céline Hoffmann,<sup>m</sup> Roland Wedlich-Söldner,<sup>n</sup> Jirí Friml,<sup>o</sup> Clément Thomas,<sup>m</sup> and Markus Geisler<sup>a,b,5</sup>

<sup>a</sup> Department of Biology, University of Fribourg, CH-1700 Fribourg, Switzerland

<sup>b</sup> Department of Plant and Microbial Biology, University of Zurich, CH-8008 Zurich, Switzerland

<sup>c</sup> CEITEC-Central European Institute of Technology, Masaryk University, CZ-625 00 Brno, Czech Republic

<sup>d</sup> Institute of Evolutionary Biology and Environmental Studies, University of Zurich, CH-8057 Zurich, Switzerland

<sup>e</sup> Max Planck Research Unit for Enzymology of Protein Folding, D-06099 Halle (Saale), Germany

<sup>f</sup> Institute of Biochemistry and Biophysics (IQUIFIB), School of Pharmacy and Biochemistry, University of Buenos Aires, C1113AAD Buenos Aires, Argentina

<sup>g</sup> Department of Enzymology, Martin-Luther-University Halle-Wittenberg, Institute of Biochemistry and Biotechnology, D-06099 Halle, Germany

<sup>h</sup> Institute of Complex Systems, ICS-6: Structural Biochemistry, D-52425 Jülich, Germany

<sup>i</sup> Centro de Biotecnología y Genómica de Plantas, 28223 Pozuelo de Alarcón, Madrid, Spain

<sup>j</sup> LINV-DIPSAA, Università di Firenze, 50019 Florence, Italy

<sup>k</sup> University of Bonn, Mulliken Center for Theoretical Chemistry, Institute for Physical and Theoretical Chemistry, D-53115 Bonn, Germany

<sup>l</sup> Plant Global Educational Project, Graduate School of Biological Sciences, Nara Institute of Science and Technology, Ikoma 630-0192, Japan

<sup>m</sup> Cytoskeleton and Cancer Progression, Laboratory of Experimental Cancer Research, Department of Oncology, Luxembourg Institute of Health, L-1526 Luxembourg, Luxembourg

<sup>n</sup> Institute of Cell Dynamics and Imaging, University of Münster, D-48149 Münster, Germany

<sup>o</sup> Institute of Science and Technology Austria, A-3400 Klosterneuburg, Austria

ORCID IDs: 0000-0002-8131-1876 (J.Z.); 0000-0002-5642-2523 (M.D.D.); 0000-0002-2981-9402 (J.O.); 0000-0003-1752-3986 (S.M.); 0000-0003-3121-2084 (N.F.); 0000-0002-8302-7596 (J.F.); 0000-0001-6720-5615 (C.T.); 0000-0002-6641-5810 (M.G.)

**Plant growth and architecture is regulated by the polar distribution of the hormone auxin. Polarity and flexibility of this process is provided by constant cycling of auxin transporter vesicles along actin filaments, coordinated by a positive auxin-actin feedback loop. Both polar auxin transport and vesicle cycling are inhibited by synthetic auxin transport inhibitors, such as 1-N-naphthylphthalamic acid (NPA), counteracting the effect of auxin; however, underlying targets and mechanisms are unclear. Using NMR, we map the NPA binding surface on the *Arabidopsis thaliana* ABCB chaperone TWISTED DWARF1 (TWD1). We identify ACTIN7 as a relevant, although likely indirect, TWD1 interactor, and show TWD1-dependent regulation of actin filament organization and dynamics and that TWD1 is required for NPA-mediated actin cytoskeleton remodeling. The TWD1-ACTIN7 axis controls plasma membrane presence of efflux transporters, and as a consequence *act7* and *twd1* share developmental and physiological phenotypes indicative of defects in auxin transport. These can be phenocopied by NPA treatment or by chemical actin (de)stabilization. We provide evidence that TWD1 determines downstream locations of auxin efflux transporters by adjusting actin filament debundling and dynamizing processes and mediating NPA action on the latter. This function appears to be evolutionary conserved since TWD1 expression in budding yeast alters actin polarization and cell polarity and provides NPA sensitivity.**

## INTRODUCTION

In land plants, virtually all developmental processes are dependent on the formation of local maxima and minima of the plant hormone auxin (Vanneste and Friml, 2009; Kania et al., 2014). These auxin gradients are created by the cell-to-cell transport of auxin, designated as polar auxin transport (PAT; Vanneste and Friml, 2009). Due to the chemical properties of the main relevant auxin, indole-3-acetic acid (IAA), PAT is thought to be established and regulated mainly by the action of precisely tuned plasma membrane auxin exporters of the PIN-FORMED and ABCB/PGP

families (Geisler and Murphy, 2006; Vanneste and Friml, 2009; Geisler et al., 2014). Both PINs and ABCBs are thought to constantly cycle between the plasma membrane (PM) and endosomal compartments associated with the trans-Golgi network, which requires the brefeldin A (BFA)-sensitive ARF-GEF (exchange factors for ARF GTPases), GNOM (Geldner et al., 2001; Cho et al., 2007; Kleine-Vehn and Friml, 2008; Titapiwatanakun et al., 2009; Wang et al., 2013). In contrast to the mainly polarly expressed PINs, widely nonpolar ABCBs are less dynamic in PM trafficking (Titapiwatanakun et al., 2009; Cho et al., 2012). However, dynamics of both auxin exporter subclasses are dependent on actin filament (AF) organization

providing tracks for secretory vesicle delivery (Geldner et al., 2001; Kleine-Vehn et al., 2006; Dhonukshe et al., 2008).

The plasma membrane presence of ABCBs is dependent on the FKBP42 (FK506 binding protein) TWISTED DWARF1 (TWD1) acting as a chaperone of endoplasmic reticulum (ER) to PM provision of ABCB1, ABCB4, and ABCB19 (Wu et al., 2010; Wang et al., 2013; Zhu and Geisler, 2015; Geisler et al., 2016). Therefore, these ABCBs, but not PIN1 or PIN2, are delocalized and degraded in *twd1* (Bouchard et al., 2006; Wu et al., 2010; Wang et al., 2013; Bailly et al., 2014). As a result, polar auxin transport is drastically reduced in *abcb1 abcb19* and *twd1*, leading to widely overlapping phenotypes, including dwarfism, disoriented growth, and helical rotation (twisting) of epidermal layers (Geisler et al., 2003; Wu et al., 2010; Wang et al., 2013). Epidermal twisting in *twd1/fkbp42* is in contrast to mutations of tubulin subunits, such as the rice (*Oryza sativa*) mutant *twisted dwarf1* (Szymanski et al., 2015), non-handed. The chaperone function of TWD1/FKBP42 is in functional analogy with the closest mammalian ortholog, FKBP38, shown to chaperone ABC7/CFTR to the PM (Banasavadi-Siddegowda et al., 2011), but underlying mechanisms are not clear.

Our knowledge on the mechanisms of PAT and auxin transporter trafficking has been expanded by the usage of synthetic auxin transport inhibitors, such as 1-*N*-naphthylphthalamic acid (NPA), a noncompetitive auxin efflux inhibitor (Cox and Muday, 1994; Butler et al., 1998). At low concentrations (1 to 5  $\mu$ M), NPA efficiently inhibits the basal polar auxin flow required for plant development. Moreover, growth of *Arabidopsis thaliana* on NPA [or its functional analog, 2-(4-diethylamino-2-hydroxybenzoyl)benzoic acid (BUM); Kim et al., 2010] induces pin-formed inflorescences phenocopying the loss-of-function mutant of the auxin exporter, *PIN-FORMED1* (*PIN1*). However, definitive data demonstrating NPA binding and direct transport inhibition for PIN proteins are lacking (Petrásek et al., 2006; Rojas-Pierce et al., 2007; Kim et al., 2010; Figure 1). Therefore, it seems obvious that NPA acts on PIN-dependent auxin transport (Petrásek et al., 2003, 2006) but by an unknown mechanism involving additional but so far not characterized regulators.

At high (>50  $\mu$ M) concentrations, NPA seems to block PAT by affecting trafficking components (Geldner et al., 2001; Gil et al., 2001; Peer et al., 2009). One mode of NPA action likely affects the actin cytoskeleton, as NPA alters AF organization, especially the extent of actin bundling. By F-actin imaging, it was demonstrated that long-term treatment with NPA (10  $\mu$ M, 48 h) decreased filamentous actin and generated punctuated structures in root epidermal cells (Rahman et al., 2007; Zhu and Geisler, 2015). The opposite effects of auxins and auxin transport inhibitors on actin bundling raised the

question of whether auxin transport inhibitors act indirectly via local accumulation of auxin concentrations (Rahman et al., 2007). However, this possibility is less likely as auxin transport inhibitors induce actin bundling in non-plant cells also (Dhonukshe et al., 2008).

Results of in vitro experiments have indicated that auxin transport inhibitors do not act on AF bundling directly (Dhonukshe et al., 2008) but rather require a not yet characterized NPA binding protein mediating the remodeling action of NPA on the actin cytoskeleton (Zhu and Geisler, 2015). Plant cells contain NPA binding proteins, although their exact number, identity, and modes of action remain surprisingly unclear (Luschnig, 2002; Zhu and Geisler, 2015). Based on biochemical in vitro assays, NPA binding proteins were reported to be PM associated, and NPA binding activity was localized to the cytoplasmic face of the membrane (Cox and Muday, 1994). Moreover, a peripheral NPA binding protein was suggested to be associated with the cytoskeleton (Cox and Muday, 1994; Dixon et al., 1996; Butler et al., 1998). ABCB-type auxin transporters and TWD1 were originally identified by NPA chromatography and subsequently verified as NPA targets (Murphy et al., 2002; Geisler et al., 2003; Rojas-Pierce et al., 2007; Nagashima et al., 2008; Kim et al., 2010). Using radiochemistry, NPA was shown to bind to the putative FKBD (FK506 binding protein domain) of TWD1 that also serves as a binding surface for ABCB-TWD1 interaction (Granzin et al., 2006; Bailly et al., 2008). Interestingly, micromolar concentrations of NPA disrupt ABCB1-TWD1 interaction, suggesting that NPA binds at the ABCB-TWD1 interface (Bailly et al., 2008).

The current picture that emerges is that auxin regulates its own transport by fine-tuning (unbundling) the organization of AFs (Holweg et al., 2004; Paciorek et al., 2005; Zhu and Geisler, 2015). Auxin transport inhibitors would counteract this effect by promoting AF bundling and subsequent auxin exporter vesicle trafficking defects and thus altered PAT (Kleine-Vehn et al., 2006; Dhonukshe et al., 2008). However, the mechanism by which auxin transport inhibitors modulate actin cytoskeleton organization remains to be explored.

Here, we searched for a functional role for NPA binding to the FKBP42, TWD1. Our data reveal that TWD1 regulates AF dynamizing and debundling processes and confers the modulatory effect of NPA on actin cytoskeleton remodeling. We precisely map the NPA binding surface on TWD1, which binds at the same time the vegetative actin subunit ACTIN7. Loss of function of *ACT7* results in mislocation of auxin exporters of PIN and ABCB subclasses and produces developmental phenotypes that are phenocopied pharmacologically by actin (de)stabilizing drugs or genetically by *TWD1* loss of function, respectively. These observations support a function for TWD1 in cytoskeleton-dependent auxin exporter trafficking in an action that seems to be evolutionary conserved and that is consistent with its previously suggested chaperone function (Wu et al., 2010; Wang et al., 2013; Zhu and Geisler, 2015).

## RESULTS

### The FK506 Binding Domain of TWD1 Binds NPA with Low Affinity, and *TWD1* Loss of Function Results in Reduced NPA Sensitivities

To identify residues of the FK506 binding protein (FKBP) domain (FKBD) of TWD1 implicated in NPA binding (Bailly et al., 2008), we

<sup>1</sup> Current address: Structural Plant Biology Laboratory, Department of Botany and Plant Biology, 1211 Geneva, Switzerland.

<sup>2</sup> Current address: Station Biologique de Roscoff, CNRS-UPMC, Place Georges Tessier, CS 90074, 29688 Roscoff, France.

<sup>3</sup> Current address: Fraunhofer Institute for Cell Therapy and Immunology IZI, Department of Drug Design and Target Validation, Halle, Germany.

<sup>4</sup> Current address: Department of Bioinformatics, Ritsumeikan University, Shiga, Japan.

<sup>5</sup> Address correspondence to markus.geisler@unifr.ch.

The author responsible for distribution of materials integral to the findings presented in this article in accordance with the policy described in the Instructions for Authors (www.plantcell.org) is: Markus Geisler (markus.geisler@unifr.ch).

www.plantcell.org/cgi/doi/10.1105/tpc.15.00726

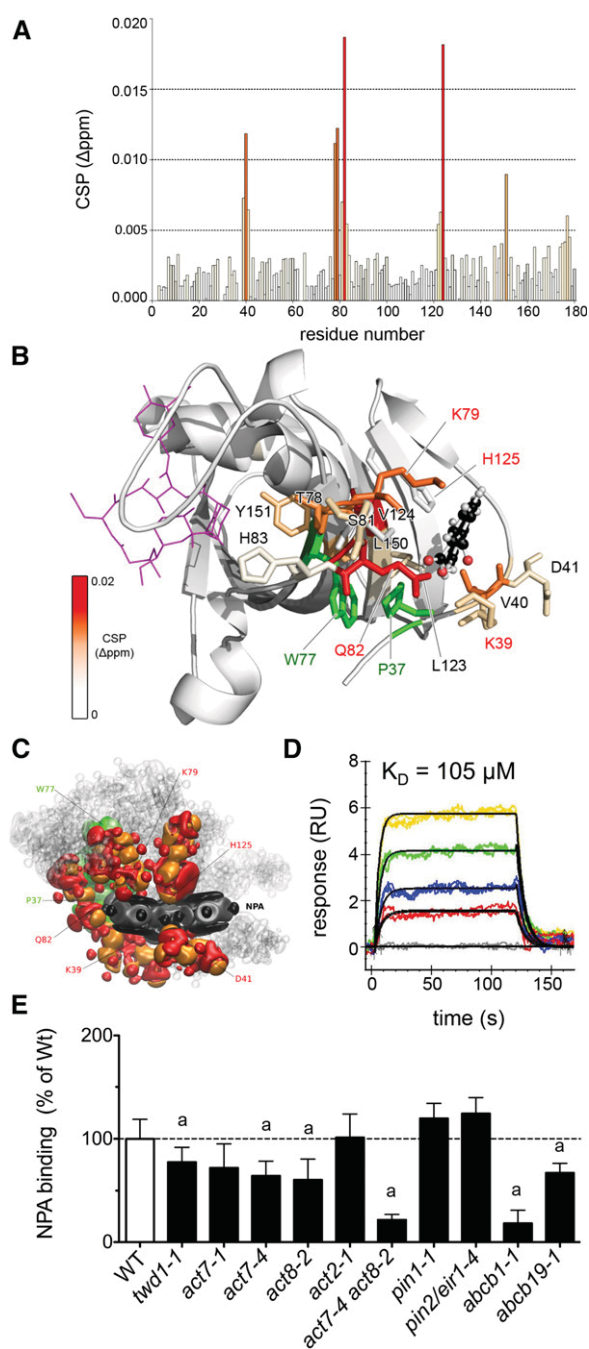


**Figure 1.** TWD1 Is a Low-Affinity NPA Binding Protein.

**(A)** NMR CSP analysis of NPA binding to TWD1<sup>1-180</sup> revealing combined <sup>1</sup>H and <sup>15</sup>N chemical shift changes. Relevant residues for the binding of NPA above 0.005 ppm are colored according to the legend in **(B)**.

**(B)** Most stable quantum chemical modeling-derived NPA-bound conformations (balls and sticks) correlate with the mapping of CSP values on FKBP42<sup>34-180</sup> (PDB ID 2IF4, color code reflects CSP shifts). Side chains of residues assumed to participate in the binding surface are depicted as sticks; relevant TWD1 mutations are in red. Theoretical FK506 binding to the noncanonical PPIase domain (PDB 1FKJ) is indicated in magenta; W77 and P37, thought to build a stacking interaction, are colored in green.

employed chemical shift perturbation (CSP) mapping based on the previously reported NMR resonance assignment of the TWD1 FKBD (Burgardt et al., 2012). Changes in the backbone amide signal positions of <sup>15</sup>N-labeled TWD1<sup>1-180</sup> in the absence and in presence of NPA were analyzed (Figure 1A; Supplemental Figure 1) and mapped onto the x-ray structure of the TWD1 FKBD (PDB 2F4E; Weiergräber et al., 2006). The most pronounced shifts were observed for residues K39, V40, D41, T78, K79, S81, Q82, H83, A122, L123, V124, and Y151, indicating that the NPA contact region is located outside of the putative PPIase (*cis-trans* peptidylprolyl isomerase) site of the FKBD at the convex face of the half  $\beta$ -barrel (Figure 1B). Quercetin, a putative auxin transport inhibitor shown not to bind to TWD1 (Bailly et al., 2008), revealed no major CSP shifts, thus indicating specificity of the binding for NPA (Supplemental Figure 1).

To corroborate the NMR data and to better understand the supramolecular NPA association with the FKBD structure, we employed *in silico* NPA docking on the entire TWD1 structure available (PDB 2IF4; Granzin et al., 2006) and on the FKBD (PDB 2F4E; Weiergräber et al., 2006) using PyMOL embedded in the AutoDock Vina toolset (Seeliger and de Groot, 2010; Bailly et al., 2011). Rigid *in silico* NPA docking followed by flexible side-chain optimization verified the FKBD as major NPA target and the predicted binding region correlates well with the one showing CSP value changes (Supplemental Figure 2).

Further, we used quantum chemical modeling based on density functional theory including dispersion correction terms (DFT-D; Effendi et al., 2015) to optimize the binding geometry of the NPA interaction using the crystal structure of the TWD1 FKBD (PDB 2F4E; Weiergräber et al., 2006) as the basis. The statistical analyses of different components of the quantum chemical forces and the electron density distribution in the region of interaction pocket-NPA deformation suggest that Van der Waals forces ( $\Delta E_{vdW}$ ) are primarily responsible for NPA binding to the TWD1 surface (Supplemental Figure 3), as has been recently proposed for other small molecule-protein interactions using thermodynamic data (Barratt et al., 2005). Furthermore, they suggest that a direct contact is provided by amino acid residues Q82, K79, H125, and D41 (Figure 1C). Strikingly, both *in silico* techniques suggest a nearly identical pocket for NPA binding and identify

**(C)** Quantum chemical analysis of the electron density components responsible for the Van der Waals forces between NPA and the surrounding amino acids. Electronic density deformation for NPA (dipole-type deformation in gray and quadrupole-type deformation in black) and for the amino acid residues (dipole-type deformation in orange and quadrupole-type deformation in red; Supplemental Figure 3).

**(D)** Kinetic analysis of NPA binding to thiol-immobilized TWD1<sup>1-339</sup>. Sensograms of injections of 15, 30, 60, and 90  $\mu$ M NPA in color and representative kinetic fit models (1:1) indicated in black. Data are representative of three independent experiments with comparable results (Table 1). Residuals and goodness-of-fit are indicated in Supplemental Figure 5. RU, normalized response units.

**(E)** Specific <sup>3</sup>H-NPA binding calculated as difference between total and unspecific NPA binding determined in the absence (total) and presence of a 1000-fold excess of nonradiolabeled NPA concentrations (unspecific). Significant differences (unpaired *t* test with Welch's correction, *P* < 0.05) from corresponding Ws and Col-0 wild types, respectively, are indicated by "a."

widely overlapping putative NPA contact residues, which are in good agreement with the NMR data (Figures 1B and 1C; Supplemental Figure 2). Furthermore, both tools revealed highly reduced internal binding energies [ $\Delta E_{\text{ave}}(\text{NPA}) = -71.65$  kJ/mol;  $\Delta E_{\text{ave}}(\text{BA}) = -31.35$  kJ/mol] and AutoDock Vina top-ranked docking pose scores (NPA =  $-11$  kcal/mol and BA =  $-4$  kcal/mol for flexible side chains mode) for benzoic acid (BA) in comparison to NPA. The former is commonly used as a negative control in auxin research and both methods exclude BA binding to TWD1 (Supplemental Figure 2).

These in vitro and in silico data allowed us to design point mutations in the putative NPA binding surface with the goal of generating a version of TWD1 that is NPA insensitive. Four out of five FKBD mutations, TWD1<sup>K79I</sup>, TWD1<sup>H125I</sup>, TWD1<sup>P37L</sup>, and TWD1<sup>K39I</sup>, abolished NPA binding (Supplemental Figure 4), which, based on chemical modeling, is mainly caused by loss of van der Waals forces ( $\Delta E_{\text{vdW}}$ ; Supplemental Figure 3) to the ligand, NPA. In TWD1<sup>P37L</sup>, NPA binding seems to be affected additionally by massive protein deformation ( $\Delta E_{\text{Pdef}}$ ) resulting in positive  $\Delta\Delta E$  and  $\Delta\Delta E_{\text{ave}}$  based on constrained geometry optimization and full geometry optimization, respectively (Supplemental Figure 3). Interestingly, TWD1<sup>Q82A</sup> revealed higher NPA binding but with lower specificity shown by BA binding assayed in parallel (Supplemental Figure 4). The latter finding is in agreement with lower calculated binding energies ( $\Delta\Delta E_{\text{ave}} = -21.43$  kJ/mol for the full geometry optimization) and the presence of very similar chemical forces in comparison to the wild-type protein according to the quantum chemical modeling (Supplemental Figure 3). TWD1 K79 was identified by NMR and both in silico dockings involved in NPA binding and TWD1<sup>K79I</sup> exhibited reduced NPA binding (in line with reduced  $\Delta\Delta E_{\text{ave}} = 6.92$  kJ/mol for the constrained geometry optimization). TWD1<sup>K79I</sup> was one of the most distant mutants in the multivariable analysis of the calculated chemical forces of the binding energies (Supplemental Figure 3) and retained its capacity to regulate ABCB1-mediated auxin transport (Supplemental Figure 4) and was therefore selected for further studies.

To test other auxin transport inhibitors for TWD1 binding, we employed surface plasmon resonance (SPR) analyses of recombinant Arabidopsis TWD1<sup>1-339</sup> protein cross-linked to sensor chips by thiol coupling. We chose this immobilization strategy over the classical amine coupling because K79 and K39 were part of the putative NPA binding surface, while TWD1 contains four cysteine residues that are outside of this domain. NPA exhibited concentration-dependent SPR responses (Figure 1D), verifying previous binding studies using radiochemistry (Bailey et al., 2008; Kim et al., 2010). Kinetic binding constants were approximated using a 1:1 Langmuir fit model, although sensograms did not always strictly follow pseudo-first-order kinetics, which was most obvious for TIBA (triiodobenzoic acid) (Supplemental Figure 5). However, dissociation constants ( $K_d$ ) obtained from both kinetic and equilibrium analyses [ $K_{d(\text{kin})} = 105 \pm 12$   $\mu\text{M}$ ,  $K_{d(\text{eq})} = 133 \pm 20$   $\mu\text{M}$ ; Table 1; Supplemental Figure 5] qualify the TWD1<sup>1-339</sup> protein as a low-affinity NPA binding protein in vitro, which is in agreement with small NMR shifts (Figure 1). Amine coupling of TWD1<sup>1-339</sup> enhanced higher order kinetic behavior of interactions and thus required a 1:2 surface heterogeneity fit model resulting in dissociation constants for NPA of 135 and 910  $\mu\text{M}$  (data not shown). This supports an inactivation of the binding surface in

a portion of the immobilized TWD1 protein, most likely by K79 and K39 coupling.

The electronic binding energy ( $\Delta E$ ) and the average of the internal energies ( $\Delta E_{\text{ave}}$ ) for NPA calculated by quantum chemical modeling ( $\Delta E = -92.56$  kJ/mol;  $\Delta E_{\text{ave}} = -71.65$  kJ/mol) cannot be precisely converted into  $\Delta G$  values. However, taking into account the dominating influence of Van der Waals interactions and therefore excluding the entropy as major binding driver, a direct transformation (see Methods for details) suggested a  $\Delta G$  between  $-20.92$  and  $-29.29$  kJ/mol. This is in agreement with the experimental SPR data, as a  $K_d$  of 105  $\mu\text{M}$  gives a theoretical  $\Delta G$  of  $-22.614$  kJ/mol (Table 1).

As expected, other auxin efflux inhibitors, like TIBA, and BUM (Kim et al., 2010) bound to TWD1, although with lower affinities (Table 1), while the unspecific diffusion control, BA, did not (Table 1; Supplemental Figure 5), verifying experimentally the in silico data.

To complement these in vitro studies, we quantified specific NPA binding to microsomes prepared from TWD1 and auxin exporter loss-of-function mutants. In agreement with low-affinity NPA binding to TWD1 and low expression of TWD1, we found slightly but significantly reduced NPA binding for *twd1* microsomes (Figure 1E). Reduced binding was also found for *abcb1* and *abcb19* material (Rojas-Pierce et al., 2007; Kim et al., 2010) but not for *pin1* and *pin2/eir1-4*, verifying the idea that direct NPA binding primarily affects the TWD1-ABCB complex (Petrásek et al., 2006; Rojas-Pierce et al., 2007; Kim et al., 2010).

In light of the above, we tested the in planta sensitivity of the *twd1* mutant toward NPA in auxin-regulated developmental processes (Bailey et al., 2008). Quantification of apical hook opening (see below), root gravitropism, and hypocotyl elongation (Supplemental Figures 6 and 7) revealed that *twd1* is widely NPA insensitive, while overexpression of HA-TWD1 in *twd1-3* complemented the NPA insensitivity of the mutant (Supplemental Figure 6).

### TWD1 Indirectly Interacts with ACTIN7

To identify downstream targets of a low-affinity, NPA-mediated TWD1 action, we employed a coimmunoprecipitation approach followed by tandem mass spectrometry (MS/MS) analyses similar to Henrichs et al. (2012) but using whole TWD1:TWD1-CFP roots as starting material. Three independent coimmunoprecipitation/mass spectrometry analyses identified 51 common, putative TWD1 interacting proteins (Supplemental Table 1). These showed a remarkable enrichment of PM proteins with a few suggested molecular functions, such as transporter activity (20%), protein binding (23%), and GTPase activity (8%; Supplemental Figure 7). Interestingly, we preferentially pulled down proteins (such as ABCB4, HSP90, ABCC1, ABCC2, and calmodulin) that either have already been shown to interact with TWD1 (Kamphausen et al., 2002; Geisler et al., 2003, 2004; Wu et al., 2010; Wang et al., 2013) or to putatively function in protein trafficking (RAB GTPases, DYNAMIN-LIKE3, CLATHRIN, and ACTIN7 [ACT7]). We selected ACT7 (score, 278; number of sequences, 9; emPAI, 1.3) for further analyses based on the following: First, ACT7 and ACT8 were previously pulled down with 35S:TAP1-TWD1 (Henrichs et al., 2012) and HA-TWD1 (data not shown) but also with ABCB1:ABCB1-MYC (data not shown), suggesting that ACT7 (and possibly also ACT8) is part of the TWD1-ABCB1 efflux complex.

**Table 1.** Kinetic Parameters Deduced from SPR Analyses Using TWD1<sup>1-339</sup>

| Compound        | $k_a$ (1/M * s) | $k_d$ (1/s)         | $K_d$ ( $\mu$ M)                                     | $\Delta G^\circ$ (kJ/mol) |
|-----------------|-----------------|---------------------|--|---------------------------|
| NPA             | 1,480 $\pm$ 238 | 0.155 $\pm$ 0.013   | 105 $\pm$ 12 (kin)                                   | -22.70 $\pm$ 0.28 (kin)   |
|                 |                 |                     | 133 $\pm$ 20 (eq)                                    | -22.14 $\pm$ 0.40 (eq)    |
| BUM             | 645 $\pm$ 35    | 0.175 $\pm$ 0.018   | 272 $\pm$ 28 (kin)                                   | -20.36 $\pm$ 0.25 (kin)   |
|                 |                 |                     | 252 $\pm$ 39 (eq)                                    | -20.56 $\pm$ 0.37 (eq)    |
| TIBA            | 290 $\pm$ 29    | 0.128 $\pm$ 0.007   | 442 $\pm$ 27 (kin)                                   | -19.15 $\pm$ 0.16 (kin)   |
|                 |                 |                     | 449 $\pm$ 34 (eq)                                    | -19.10 $\pm$ 0.19 (eq)    |
| BA <sup>a</sup> | 543 $\pm$ 501   | 14.318 $\pm$ 12.270 | 33,097 $\pm$ 11,077 (kin)                            | -8.55 $\pm$ 0.87 (kin)    |
|                 |                 |                     | 1.4 10 <sup>19</sup> $\pm$ 4.4 10 <sup>18</sup> (eq) | 75.00 $\pm$ 0.73 (eq)     |

Double referencing and data analysis were performed using Scrubber2 (BioLogig Software) and TraceDrawer (Ridgeview Instruments) analysis software. Affinity binding constants ( $K_d$ ) were obtained by equilibrium analysis [ $K_{d(eq)}$ ] and by least-squares nonlinear fit of the obtained sensograms using a 1:1 Langmuir binding model [ $K_{d(kin)}$ ], which additionally allowed for the evaluation of dissociation ( $k_d$ ) and association ( $k_a$ ) rate constants. Values represent means and standard deviations of kinetic constants obtained from at least three experiments on independent sensor chips. Corresponding sensograms and fit models are shown in Supplemental Figure 5.

<sup>a</sup>Sensograms obtained for BA did not allow for a meaningful fit, indicating that TWD1<sup>1-339</sup> did not bind BA.

Second, *ACT7* is strongly expressed in young plant tissues and is induced by auxin, and *act7* alleles cause a reduction in root growth and increased root slanting and waving, resembling the *twd1* mutant phenotype (Kandasamy et al., 2009).

Identification of ACT7 as a TWD1 interactor does not necessarily imply direct physical interaction. To assess the ability of TWD1 to autonomously bind AFs and to map the potential actin binding region, high-speed cosedimentation assays were conducted with TWD1<sup>1-180</sup> (FKBD) and TWD1<sup>1-339</sup> and rabbit muscle actin in various conditions of calcium and pH (Papuga et al., 2010). As exemplified for FKBD (Supplemental Figure 9A), both the truncated and full-length proteins mostly remained in the supernatant fraction, and only a faint amount (<5%) was detected in the pellet fraction together with AFs. Because a similar portion of TWD1<sup>1-180</sup> and TWD1<sup>1-339</sup> also sedimented in control experiments (i.e., without actin), we considered it as being unspecific. As an additional indication that TWD1 does not interact with AFs in a direct manner, it had no effect on the actin polymerization rate in pyrene-actin assays conducted in the absence or presence of NPA (Supplemental Figure 9B).

### TWD1 Regulates Actin Cytoskeleton Organization and Dynamics and Mediates the Effect of NPA on AF Turnover

To gain insight into a putative functional link between TWD1 and the actin cytoskeleton, we carefully examined actin filament organization in wild-type and *twd1-1* seedlings in which we introduced the actin reporter GFP-fABD2 (Sheahan et al., 2004). Employing variable-angle epifluorescence microscopy (VAEM), we noticed that, compared with wild-type hypocotyls, *twd1-1* exhibited fewer thick and bright filamentous structures corresponding to actin bundles (Figure 2). To confirm and extend these data, actin filament bundling (skewness) and density (percentage of occupancy) were quantified in the hypocotyl epidermal cells from dark-grown seedlings following established protocols (Higaki et al., 2010). Average skewness values of  $2.84 \pm 0.05$  and  $2.29 \pm 0.06$  were calculated for wild-type and *twd1-1* hypocotyls, respectively (Figure 2B), confirming that loss of TWD1 lowers the overall cellular level of actin bundling. In addition, and most likely

as a result from reduced actin bundling, actin filament density was increased in *twd1-1* (Figures 2A and 2C). Interestingly, long-term treatment with NPA (10  $\mu$ M, 5 d after germination [dag]) induced prominent cytoskeletal changes in wild-type hypocotyls with a 40% increase in actin bundling and 35% decrease in actin filament density (Figures 2A to 2C), similar to what has been reported before for the auxin transport inhibitors 2-(1-pyrenoyl) benzoic acid (PBA) and TIBA (Dhonukshe et al., 2008). The absence of an effect of NPA on actin stability in previous studies might be due to shorter treatments and/or a lower microscopic resolution compared with our VAEM analyses (Petrásek et al., 2003; Dhonukshe et al., 2008).

In striking contrast to the wild type, NPA had no significant effect on actin filament bundling and density in *twd1-1* hypocotyls (Figures 2A to 2C), indicating that NPA-mediated actin bundling requires TWD1. Interestingly, *act7-4* hypocotyls exhibited excessive bundling compared with the wild type. However, like in *twd1-1*, the extent of actin bundling was insensitive to NPA, further supporting a functional TWD1-ACT7 interaction. The NPA resistance of *twd1-1* and *act7-4* hypocotyls was confirmed using standard confocal microscopy analyses of identical GFP-fABD2 lines (Supplemental Figure 10 versus Figure 2) using described methods (Higaki et al., 2010). We found that *twd1-1* and *act7-4* were insensitive to NPA in tested concentrations up to 100  $\mu$ M, while bundling reached already a saturation at 10  $\mu$ M NPA in the hypocotyls of wild-type and *twd1-1* hypocotyls complemented by TWD1:TWD1-CFP (Supplemental Figure 11). The bundling defects caused by low micromolar NPA concentrations in wild-type hypocotyls might at first view seem contradictory to the relatively high  $K_d$  value ( $\sim$ 105  $\mu$ M) that we obtained by SPR analyses. However, it is likely that NPA accumulates within tissues and can locally reach high concentrations, especially after long-term treatments as those used in our culture conditions. Moreover, binding affinities generated in vitro might considerably differ from those in planta.

In addition to the static analyses above, we quantified several parameters of single actin filament dynamics (Staiger et al., 2009; Henty-Ridilla et al., 2013; Hoffmann et al., 2014b). In the wild type, cortical AFs exhibited typical dynamics including a relatively short lifetime ( $31 \pm 7.4$  s), and high elongation rate and severing

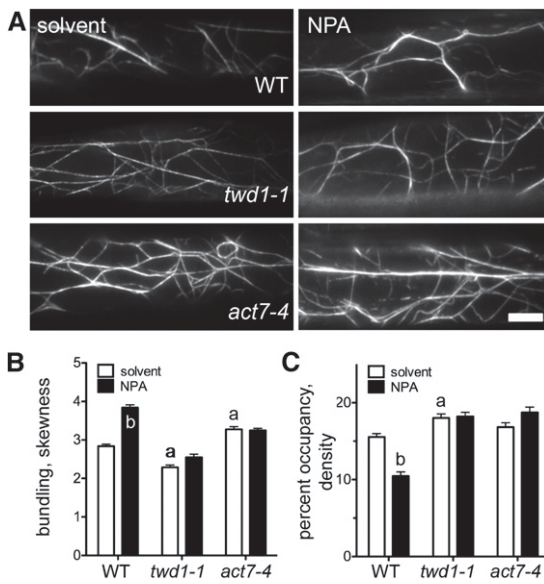


**Figure 2.** Actin Architecture and NPA Sensitivity Is Altered in *twd1-1*.

Time-lapse VAEEM analyses of cortical actin of dark-grown hypocotyl expressing fABD2-GFP treated with 1  $\mu$ M NPA. Representative epidermal cells (**A**) and quantification of actin bundling (skewness; **B**) and percentage of occupancy (density; **C**). Significant differences (unpaired *t* test with Welch's correction,  $P < 0.05$ ) between wild-type and mutant alleles are indicated by "a" and significant differences to solvent controls by "b" (mean  $\pm$  SE;  $n \geq 100$ ). Bar = 10  $\mu$ m.

frequency ( $2.9 \pm 1.0$   $\mu$ m/s and  $0.011 \pm 0.004$  breaks/ $\mu$ m/s, respectively; Table 2) that are in good agreement with previous data (Henty et al., 2011). In *twd1-1*, actin filament lifetime was significantly higher than in the wild type with an average of  $45.1 \pm 10.3$  s. This increase in actin filament stability was consistent with a reduced depolymerization rate and severing frequency (Supplemental Movies 1 to 3). NPA treatment altered virtually all parameters of actin filament dynamics in wild-type hypocotyls. Consistent with the fact that NPA increases the overall level of actin bundling (Figure 2), it lowered actin filament dynamics as shown by an increase in actin filament lifetime and length and a decrease in actin filament severing (Supplemental Movies 4 to 6). Most remarkably, and in agreement with the inability of NPA to promote actin bundling in *twd1-1* hypocotyls, none of the single actin filament dynamic parameters analyzed was affected by NPA treatment in *twd1-1* (Table 2).

Our data revealed that bundling frequencies of AFs were similar in wild-type and *twd1-1* hypocotyls (Table 2). By contrast, debundling frequency was much (nearly 4 times) higher in *twd1-1*, which seems to account for the reduced overall bundling level observed in *twd1-1* hypocotyls (Figure 2). Thus, it appears that TWD1 triggers a dual action on actin cytoskeleton organization and dynamics in hypocotyls: On one hand, it stimulates single AF dynamics, e.g., by increasing AF depolymerization and severing, and on the other, it downregulates the process of debundling. Surprisingly, NPA reduced actin bundling and debundling frequencies by  $\sim 50\%$  in both wild-type and *twd1-1* hypocotyls (Table 2). This unexpected result suggests that, in addition to its

TWD1-dependent action on single AF dynamics, NPA may modulate the processes of actin bundling/debundling in a TWD1-independent manner. Consistent with the fact that actin bundling and debundling frequencies were similarly reduced by NPA, NPA treatment had no apparent effect on the overall actin bundling level and AF density in *twd1-1* (Figures 2B and 2C; Supplemental Figures 10B and 11B).

### ACT7 Regulates Expression and Location of ABCB- and PIN-Type Auxin Exporters as well as TWD1

The known role of the actin cytoskeleton in auxin transporter cycling (Geldner et al., 2001; Kleine-Vehn et al., 2006; Dhonukshe et al., 2008) and delocalization of ABCBs in *twd1* (Wu et al., 2010; Wang et al., 2013) prompted us to investigate the locations of auxin transporters in *act7-4*. We found that expression of ABCB1-GFP and ABCB19-GFP and, most drastically, ABCB4-GFP was significantly downregulated in *act7-4* and that all tested ABCBs were partially retained on intracellular structures (Figures 3 and 4). PIN1-GFP and PIN2-GFP were likewise found on similar structures and their polarity was reduced (Figures 3 and 4). However, in contrast to ABCBs, expression of PIN2 was less affected, while expression of PIN1 was even slightly upregulated (Figure 3C). To our surprise, TWD1-CFP was also partially delocalized from ER/PM locations in *act7-4* (Figure 3B), which is in line with the proposed chaperone function of TWD1 during ER-to-PM secretion of ABCBs (Wu et al., 2010; Wang et al., 2013). Moreover, TWD1 lost lateral PM polarity (Wang et al., 2013) in immunostained roots of *act7* single and double loss-of-function mutant material (Supplemental Figure 12). We noticed that both endosomal structures and transporter delocalizations in *act7-4* were often found in misshaped cells (Figures 3 and 4). A thorough investigation employing PIN2-GFP and propidium iodide staining of cell walls revealed that these defects indeed are found in misshaped cells but that they do not strictly correlate with cell wall defects (Figures 3 and 4). Delocalizations for PIN1,2-GFP and ABCB4-GFP were also not caused by nonisogenic ecotype backgrounds (see Methods for details) as revealed by immunolocalization of PIN1,2 in *act7-4* and crossings between ABCB4-GFP and *act7-6* lines that are both in the Col-0 background (Supplemental Figure 13).

Short treatments with endocytic tracer FM4-64 (2  $\mu$ M, 15 min) resulted in FM4-64 accumulation into internal (probably TGN or early endosomal) structures in *act7-4* and, more severely, in actin double mutants, but not in *twd1* (Supplemental Figure 12A), suggesting a role for ACT7 in endosomal balance. An early endosomal/TGN marker, ARF1, showed a similarly defective distribution in *act7-4* and *act7-4 twd1-1* but not in *twd1-1*, verifying the endosomal identity of defective endomembranes (Supplemental Figure 12B). LysoTracker red (LTR) and long-term FM4-64 (4  $\mu$ M, 3 h) applications revealed additionally aberrant vacuolar morphologies (Supplemental Figures 12C and 12D), while crossings of *act7-4* with lines expressing endosomal/prevacuolar markers RabF1/ARA6, Syp22, and Syp61 revealed intracellular localization defects (Supplemental Figure 14).

These findings encouraged us to colocalize ABCB4/ABCB19 and PIN1/PIN2 with different endosomal and vacuolar markers in *act7-4*. ABCB4, ABCB19, and PIN2 (but not PIN1) showed

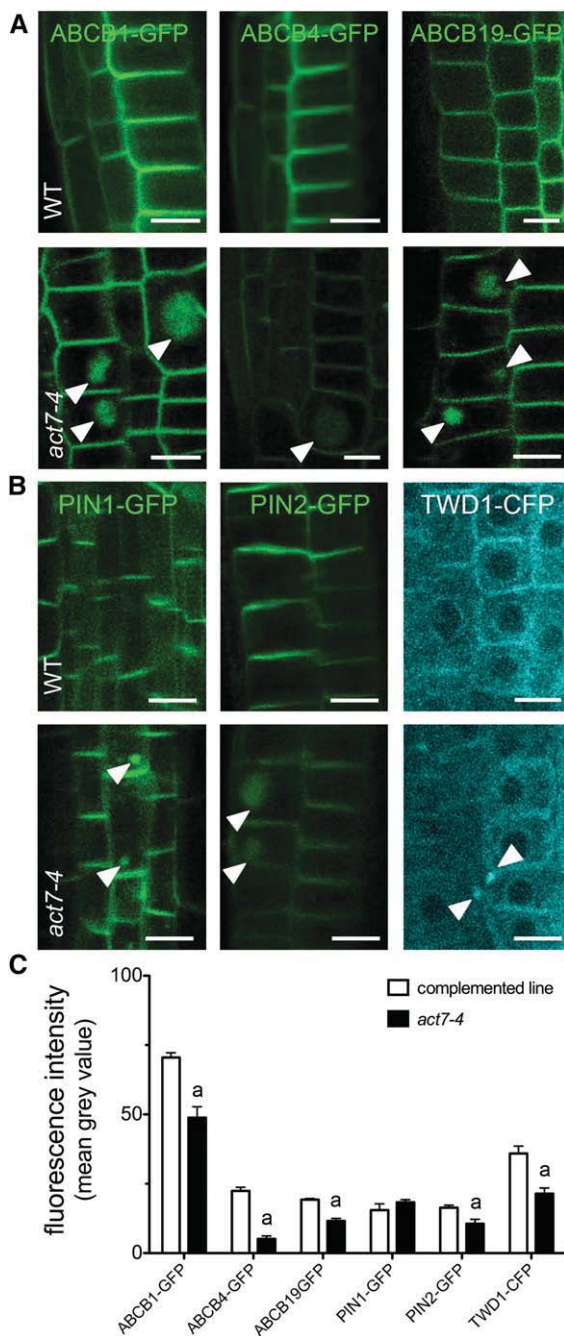


**Figure 3.** ACT7 Regulates ABCB- and PIN-Type Auxin Transporter as well as TWD1 Expression and Location.

**(A)** and **(B)** Auxin transporters, ABCB1,4,19-GFP **(A)** and PIN1,2-GFP, as well as the ABCB chaperon, TWD1-CFP **(B)**, are delocalized from the root PM and ER, respectively, retained on punctuated structures (arrows), and significantly downregulated in *act7-4* in comparison to the corresponding wild-type lines. Bars = 10  $\mu$ m.

**(C)** Quantification of **(A)** and **(B)**. Significant differences (unpaired *t* test with Welch's correction,  $P < 0.05$ ) between the wild type and *act7-4* are indicated by "a" (mean  $\pm$  SE;  $n \geq 50$  images). Note that GFP quantifications by confocal imaging were performed over identically defined areas of the entire root tip and therefore quantified intensities in **(C)** might not match

increased colocalization with FM4-64 after long-term treatments (Figures 4A and 4B) and with the vacuolar marker LTR in *act7-4* (Figures 4C and 4D), while PIN1 revealed already a high colocalization factor in the isogenic wild-type background. These data suggest a mislocalization of both classes of auxin exporters on compartments of vacuolar/late endosomal origin in *act7-4*. To address further the nature of these structures, we performed short BFA treatments (25  $\mu$ M, 1 h) of PIN1-GFP and ABCB19-GFP lines and found that both colocalize with PM marker, FM4-64, on BFA compartments in the wild-type background and *act7-4*. In *act7-4*, PIN1-GFP and ABCB19-GFP were retained on BFA bodies on additional compartments with putative late endosomal-like nature (Supplemental Figure 15). These data support further retention of both classes of auxin exporters on compartments of endosomal/vacuolar origin in *act7-4*.

### *twd1* and *act7* Show Overlapping Developmental Phenotypes That Are Caused by Defects in Polar Auxin Transport

Arabidopsis contains eight ACTIN genes that are grouped into reproductive and vegetative classes; the latter class contains ACT2, ACT7, and ACT8 (Kandasamy et al., 2009). ACT7 mutant combinations are dwarfed, with altered cell and organ morphology, suggesting that ACT7 is involved in root growth, epidermal cell specification, cell division, and root architecture (Kandasamy et al., 2009). The actin defects in *twd1* and auxin transporter delocalizations in *act7* stimulated us to compare in detail auxin-regulated phenotypes in *twd1* and *act7*, with special focus on tissues and processes related to actin-dependent growth.

A hallmark of the *twd1* phenotype is a non-handed, helical rotation (twisting) of epidermal layers that can be (like in *abcb1 abcb19*) partially rescued by NPA treatment (Geisler et al., 2003; Wu et al., 2010; Bailly et al., 2014; Figure 5A). Interestingly, we found that both *act7* alleles and mutant combinations with *act7*, but not *act2-1* or *act8-2*, also show substantial epidermal twisting that was, however, NPA insensitive (Figure 5A). Next, we analyzed the planar polarity of root hair positioning, which is determined by a concentration gradient of auxin distribution in the root tip (Grebe, 2004). This gradient itself is regulated by upstream events, such as polar placement of ROP (Rho-of-plant) GTPases or auxin transporter activity (Masucci and Schiefelbein, 1994; Grebe, 2004). Surprisingly, *twd1-1* and both *act7* alleles showed a striking apical shift in root hair positioning that was strongest in *act7-4 twd1-1* and *act7-4 act8-2* (Figure 5B). Defects in planar root hair polarity have also been reported very recently for two new ACT7 alleles shown to influence ROP positioning (Kiefer et al., 2015). In analogy to epidermal twisting, root hair positioning was only mildly disturbed in *act2-1* and *act8-2*. NPA treatment of wild-type phenocopied *twd1* and *actin* alleles, but again *twd1* was found to be widely NPA insensitive, while *actin* mutants were even partially rescued (Figure 5B).

pictures in **(A)** and **(B)**. Furthermore, PIN1,2-GFP and ABCB4-GFP non-isogenic lines were used for analyses in *act7-4* but artifacts caused by ecotype mixes were excluded by immunolocalizations or isogenic controls (Supplemental Figure 13).

**Table 2.** Parameters of Actin Dynamics Deduced from Time-Lapse VAEM Analyses of Single, Cortical Actin Filaments of Arabidopsis Hypocotyls Expressing fABD2-GFP

| Parameter  | Wild Type  |   | <i>twd1-1</i>                                    |   |
|--|--|---|--|---|
|  | –NPA <sup>a</sup>                                | +NPA <sup>b</sup>                                 | –NPA <sup>c</sup>                                | +NPA <sup>d</sup>                                 |
| Max. filament lifetime (s)                       | 31.1 ± 7.4                                       | 47.0 ± 15.7**                                     | 45.1 ± 10.3*                                     | 44.3 ± 11.3                                       |
| Max. filament length (μm)                        | 27.9 ± 9.9                                       | 33.2 ± 14.5**                                     | 28.2 ± 10  | 28.5 ± 9.1  |
| Elongation rate (μm/s)                           | 2.9 ± 1.0  | 3.4 ± 1.3**                                       | 2.9 ± 0.9  | 3.0 ± 1.0   |
| Depolymerization rate (μm/s)                     | 1.4 ± 0.7  | 1.1 ± 0.8   | 0.9* ± 0.4                                       | 0.9 ± 0.3   |
| Severing frequency (breaks/μm/s)                 | 0.011 ± 0.004                                    | 0.008 ± 0.003**                                   | 0.009* ± 0.003                                   | 0.008 ± 0.003                                     |
| Bundling frequency (events/μm <sup>2</sup> /s)   | 1.640 10 <sup>-4</sup> ± 1.324 10 <sup>-6</sup>  | 0.883 10 <sup>-4</sup> ± 0.645 10 <sup>-6**</sup> | 1.890 10 <sup>-4</sup> ± 1.314 10 <sup>-6</sup>  | 0.872 10 <sup>-4</sup> ± 0.999 10 <sup>-6**</sup> |
| Debundling frequency (events/μm <sup>2</sup> /s) | 0.590 10 <sup>-4</sup> ± 0.2445 10 <sup>-5</sup> | 0.280 10 <sup>-4</sup> ± 0.194 10 <sup>-5**</sup> | 1.910 10 <sup>-4</sup> ± 0.414 10 <sup>-5*</sup> | 0.910 10 <sup>-4</sup> ± 0.264 10 <sup>-5**</sup> |

Shown are means ± SE of 127 filaments from 34 cells.

<sup>a</sup>Ninety-nine filaments from 31 cells.

<sup>b</sup>Ninety-six filaments from 41 cells.

<sup>c</sup>Ninety-six filaments from 46 cells.

<sup>d</sup>Significant differences (unpaired *t* test with Welch's correction; *P* value < 0.01) to wild-type or solvent controls are indicated by \* and \*\*, respectively.

Finally, we analyzed leaf trichome branching, which usually displays a variation between one and four branches in wild-type plants (Hülkamp et al., 1994). Both *act7* alleles exhibited a significant shift toward dibranched trichomes (Figure 5C), as previously reported for *act2 act7* double mutants (Kandasamy et al., 2009). Strikingly, *act7-4* and *twd1-1* showed largely identical trichome branching patterns, which were even more radical in *act7 twd1* and *act2 act7*, again resembling NPA treatments (Grebe, 2004).

To link auxin-related phenotypes to actin function, we employed the actin destabilizing and stabilizing drugs, latrunculin B and jasplakinolide, shown to reduce the elongation rate and to induce actin polymerization, respectively (Staiger et al., 2009). Like NPA, latrunculin B and jasplakinolide treatments were able to block apical hook formation in etiolated wild-type seedlings (Figure 5D) known to be dependent of a local accumulation of auxin at the inner side of the hook (Zádníková et al., 2010). Interestingly, *twd1* hooks were less sensitive to NPA and latrunculin B treatments than the wild type but not to jasplakinolide, most probably due to already reduced actin bundling (Figure 2B). *act7-4* was fully responsive to all treatments, further underlining functional redundancy between vegetative actin isoforms (Kandasamy et al., 2009).

Latrunculin B and jasplakinolide had a similar inhibitory effect on hypocotyl elongation as NPA in the wild type, and like for hook opening, *twd1-1* but not *act7-4* was greatly insensitive (Supplemental Figure 7A). Interestingly, paclitaxel/taxol and oryzalin, well-established stabilizers and inhibitors of microtubule polymerization, similarly affected hypocotyl length in *twd1-1* (and *act7-4*) in comparison to the wild type (Supplemental Figure 7B), making an involvement of TWD1 (and ACT7) in microtubule-related cell elongation unlikely.

Overlapping auxin-related growth phenotypes between *act7* and *twd1* mutants support a tight mechanistic link between actin dynamics and auxin efflux (Muday, 2000; Blancaflor et al., 2006; Dhonukshe et al., 2008). This prompted us to quantify auxin responses and transport in *act7* mutants. Activation of the

auxin-responsive DR5rev:GFP reporter (Friml et al., 2003) was slightly reduced in the *act7-1* allele but more drastically in the *act7-4* root tip, as has been reported before for *twd1-1* (Figures 6A and 6B; Bouchard et al., 2006). Interestingly, latrunculin B and jasplakinolide treatments phenocopied TWD1 and ACT7 loss of function, implying that these drugs also cause PAT defects. In agreement, free IAA levels were significantly elevated in *act7-4* and *twd1-1* roots (Figure 6C; Bouchard et al., 2006).

Finally, we employed a self-referencing IAA-specific micro-electrode that permits continuous, noninvasive recordings of distinct IAA flux peaks in the epidermis of the apex of Arabidopsis roots (Mancuso et al., 2005; Henrichs et al., 2012), correlating with a PIN-dependent auxin “reflux loop” from peripheral root cells toward central vascular cells (Blilou et al., 2005). Latrunculin B and jasplakinolide treatments (each 5 μM) blocked root PAT as efficiently as NPA (Bailly et al., 2008), which is genetically copied by loss of ACT7 function (Figures 6D and 6E). Interestingly, root auxin fluxes into *act7-4* roots show reduced sensitivities to latrunculin B and jasplakinolide (Supplemental Figure 16), resembling *twd1*, which is insensitive to NPA (Bailly et al., 2008).

In summary, these data sets support the concept that either destabilization or stabilization of the actin cytoskeleton causes PAT defects to a similar magnitude as reported for NPA treatments. Overlapping growth phenotypes and PAT defects caused either by chemical actin (de)stabilization or by TWD1 or ACT7 mutations suggest that abnormal actin cytoskeleton function in *twd1* is the primary reason for PAT defects, which are likely to be the cause of previously overlooked developmental defects in *twd1*.

#### Expression of TWD1 in Yeast Alters Budding and Actin Polarity and Confers NPA Sensitivity

With the apparent conserved FKBP functionality in mind, we phenotypically characterized wild-type budding yeast expressing

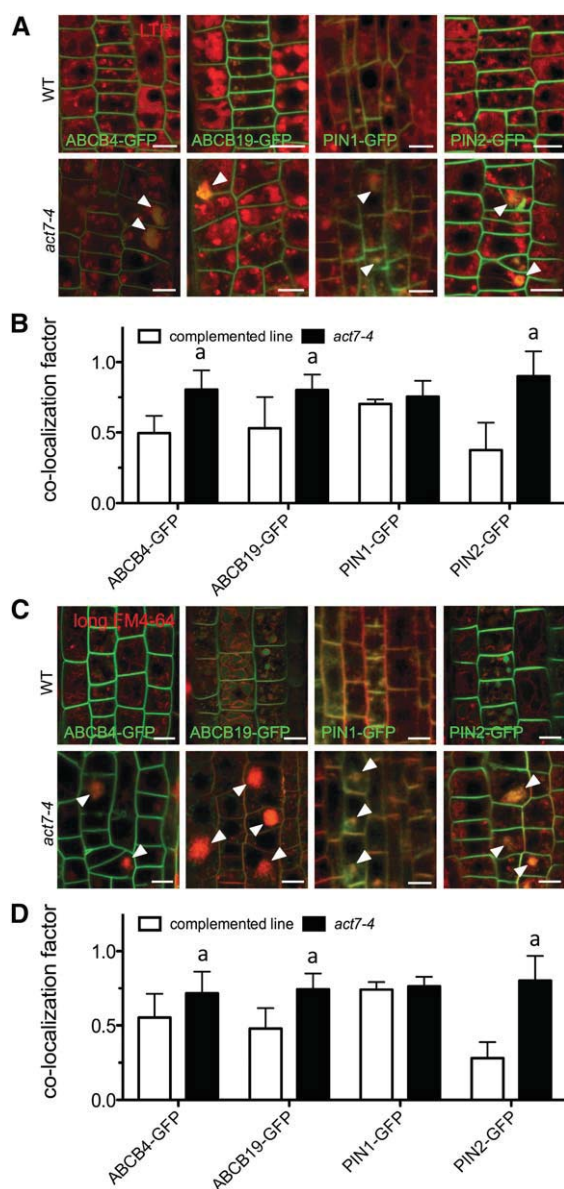


**Figure 4.** ABCB- and PIN-Type Auxin Exporters Colocalize with Vacuolar Markers in *act7-4*.

**(A)** ABCB4-GFP, ABCB19-GFP, PIN1-GFP, and PIN2-GFP colocalize (arrows) with compartments stained after long FM4-64 treatments (4  $\mu$ M, 3 h) in *act7-4*, indicating vacuolar origin.

**(B)** and **(D)** Quantification of ABCB and PIN colocalization in the wild-type and *act7-4* with FM4-64 **(B)** and LTR markers **(D)**. Significant differences (unpaired *t* test with Welch's correction,  $P < 0.05$ ) between the wild type and *act7-4* are indicated by "a" (mean  $\pm$  SE;  $n \geq 50$  images).

**(C)** ABCB19 and PIN1, and to a lesser extent ABCB4 and PIN2, colocalize with late vacuolar marker, LTR, in *act7-4*. Bars = 10  $\mu$ m.

Arabidopsis TWD1 and found that these yeasts held a significant higher population of large-budded cells compared with those harboring the vector control, while the amount of unpolarized cells stayed constant (Figures 7A and 7B). NPA completely reverted this promotional effect of TWD1 on large buds, while the vector control

was NPA insensitive. Interestingly, the TWD1<sup>K79I</sup> mutant shown above to be unable to bind NPA but still capable of regulating ABCB1 activity (Supplemental Figure 4) had the same effect on yeast polarization as wild-type TWD1 but was, as expected, NPA insensitive. However, expression of the strong NPA binder TWD1<sup>Q82A</sup> increased accordingly the number of nonpolarized cells but was also NPA insensitive, suggesting that this mutant fails to complete downstream signaling.

In an unbudded cell, actin cables and patches are distributed randomly, but during budding, actin cables become bundled and are polarized toward the budding site (Casamayor and Snyder, 2002). To connect the growth phenotypes caused by TWD1 with a putative effect of TWD1 on the yeast cytoskeleton, we quantified the percentage of yeast with polarized actin by staining actin filaments with phalloidin-Alexa Fluor 488. Yeast expressing TWD1 revealed a significantly higher amount of actin polarization in unbudded cells in comparison to the vector control, while actin in large-budded TWD1 cells was less polarized (Figure 7C). In agreement with budding analyses, expression of TWD1<sup>K79I</sup> altered actin polarization in large buds and as expected did not convey NPA sensitivity to this process.

An unexpected finding was that expression of TWD1 and TWD1<sup>K79I</sup> increased the cell size of mother cells and buds significantly, independently from their actin polarization status (Supplemental Figure 17). Surprisingly, increased cell size was exaggerated by NPA treatments, however, in an action that was TWD1 independent.

As actin polarization and connected vesicle transport forms the basis for yeast budding, our yeast data provide evidence that growth defects in yeast expressing TWD1 are triggered by altered actin polarization. They also indicate that the effect of TWD1 on the actin cytoskeleton is evolutionarily conserved, as was demonstrated for the function of auxin transport inhibitors on actin (Dhonukshe et al., 2008). However, in this study, NPA was less effective in promoting actin bundling in comparison to TIBA or PBA, most probably due to a lack of an appropriate NPA target. Deletion of all four FKBP, *FPR1-4*, in the yeast strain KDY81.18c (Hemenway and Heitman, 1996) significantly reduced budding (Supplemental Figure 17B) similarly as was found for expression of TWD1<sup>Q82A</sup>. However, the finding that size in the *fpr1-4* yeast was not affected by NPA suggests that the effect of NPA on yeast size is provided by yeast-endogenous FKBP, further supporting an evolutionary conservation of this individual function.

## DISCUSSION

Inhibitors of auxin export, with NPA being the most prominent, have been widely used in plant biology for almost a century and have greatly contributed to our understanding of the mechanisms of auxin-mediated plant development. Besides inhibiting auxin transport directly, auxin transport inhibitors at higher concentrations also alter actin stability (Rahman et al., 2007; Dhonukshe et al., 2008; this study) and vesicle trafficking (Geldner et al., 2001); however, their mode of action and molecular targets are still remarkably unclear (Luschnig, 2001; Muday and Murphy, 2002; Dhonukshe et al., 2008; Zhu and Geisler, 2015). Finally, it is unknown if the effects of auxin transport inhibitors on the actin

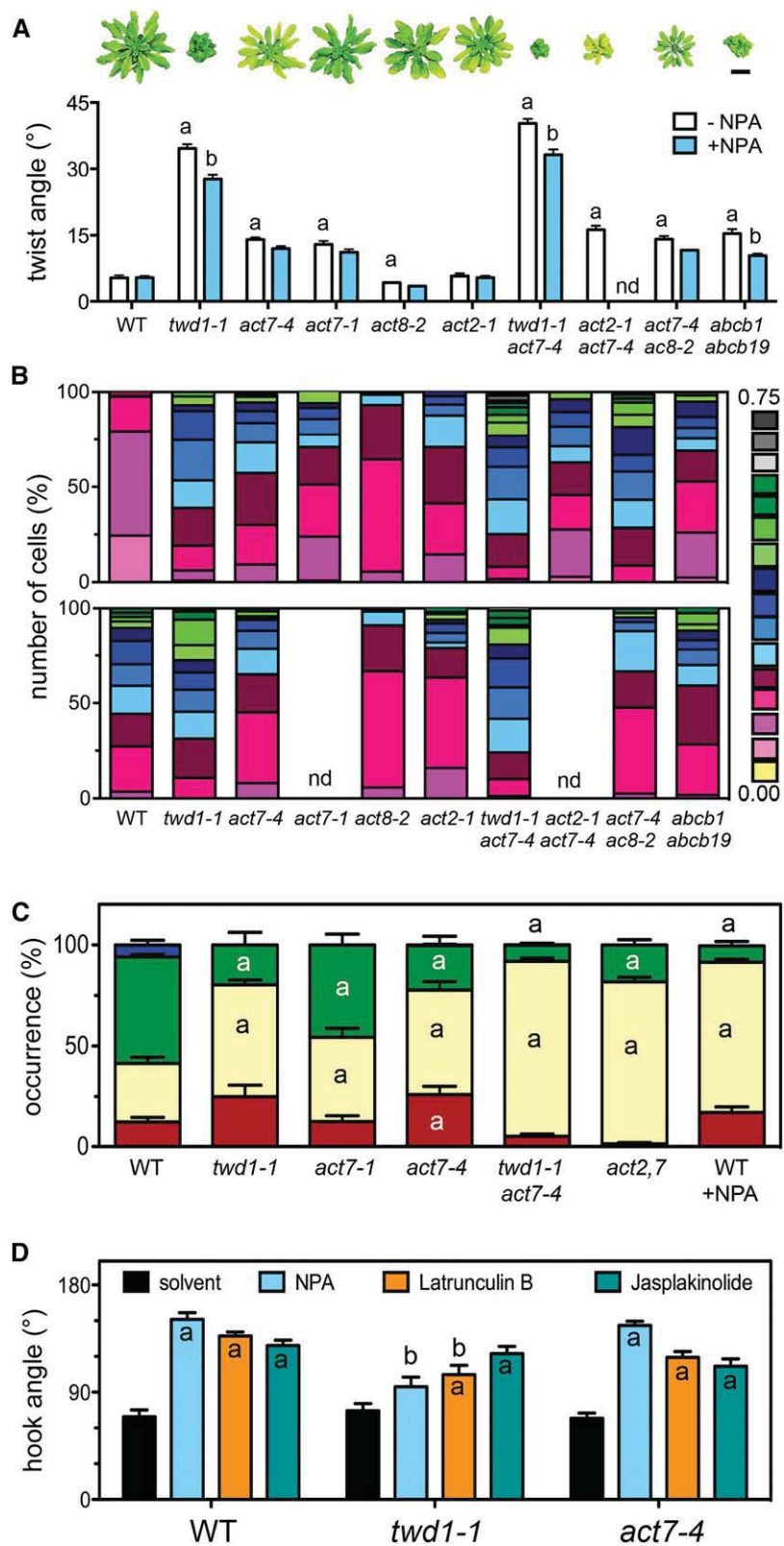


Figure 5. *twd1* and *act7* Show Overlapping Developmental Phenotypes.

cytoskeleton, vesicle trafficking, and auxin transport are directly connected.

In this study, we characterized the FKBP42 TWD1 as a low-affinity binding protein for established auxin transport inhibitors, including NPA. We precisely mapped the NPA binding surface outside of the putative PPlase/FK506 binding site of the FKBD (Figure 1; Supplemental Figure 2). Drug binding to this subdomain might offer a justification for the atypical structural FKBP clamp (residues S31 to A44) in TWD1 that is thought to be held in place by a stacking interaction between the rings of W77 and P37 (Figure 1B; Burgardt et al., 2012). In agreement, mutation of P37 drastically alters protein stability (Supplemental Figure 3). Notably, the NPA contact region on TWD1 corresponds quite closely to the interaction site in the modeled complex between TWD1 and the second nucleotide binding domain of ABCB1 (Granzin et al., 2006), providing a mechanistic explanation for the finding that micromolar concentrations of NPA are sufficient to disrupt TWD1-ABCB1 interaction (Bailey et al., 2008). In summary, it appears as if the N-terminal FKBD might have lost its originally conserved PPlase activity toward a functionality that serves as a platform for multiple protein-protein interactions that are modulated by regulatory drugs, such as NPA.

TWD1 physically and functionally interacts with structural actin cytoskeleton components (here, ACT7; Supplemental Figure 7 and Supplemental Data Set 1). Moreover, our live-cell imaging analyses established that TWD1 influences both actin bundling and actin filament dynamics at the cortex of hypocotyl epidermal cells (Figure 2, Table 2). This role for TWD1 and physical interaction with ACT7 is in line with previous *in vitro* and *in vivo* data supporting the concept that a peripheral NPA binding protein is associated with the cytoskeleton (Cox and Muday, 1994; Dixon et al., 1996; Butler et al., 1998). This holds especially true in light of evidence indicating that TWD1 is attached to the PM via an in-plane membrane anchor (Scheidt et al., 2007; Bailey et al., 2014). Indirect support for this concept also comes from the finding that NPA binding capacities are reduced in *twd1*, *act7*, and *act8* but not in *act2* (Figure 1E), which, based also on our phenotypical analyses (Figure 5), seems to own a distinct function. Recently, ACT2 was shown to integrate BR signaling and BR-mediated auxin responses (Lanza et al., 2012). A distinct functionality for ACT2 is further supported by the finding that *act2-5* roots revealed reduced actin filament skewness similar to brassinosteroid or auxin

treatments (Lanza et al., 2012), while *act7-4* and NPA treatments had opposite effects (Figure 2).

Stabilization of actin bundles and, thus, regulation of vesicle dynamics by several auxin transport inhibitors is conserved among plant, yeast, and mammalian cells (Dhonukshe et al., 2008). In agreement with our data (Figure 7), previous work failed to demonstrate an effect on actin bundling for NPA in yeast, while PBA and TIBA were effective (Dhonukshe et al., 2008). Expression of TWD1 specifically fostered yeast budding most likely as a consequence of TWD1-mediated polarization of actin filaments (Figure 7), serving as cargo tracks for polar vesicle delivery to new buds (Casamayor and Snyder, 2002). Importantly, this action was reverted by NPA, while vector-control yeast was NPA insensitive, indicating that TWD1 is responsible for NPA sensitivity (Figure 7). Further support is provided by the fact that the non-NPA binder, TWD1<sup>K79I</sup>, widely retains its ability to regulate actin polarization and yeast budding but does not confer NPA sensitivity.

In agreement with an actin filament bundling role for TWD1, the PM presence of auxin efflux transporters is seriously distorted in *twd1* (Wu et al., 2010; Wang et al., 2013) but also in *act7* (Figures 3 and 4). While the role of TWD1 as a chaperone during ER-to-PM secretion seems to be specific for ABCBs (Bouchard et al., 2006; Wu et al., 2010; Wang et al., 2013), both PINs and ABCBs are retained at early endosomal/vacuolar compartments in *act7* (Figure 4). Based on marker and BFA analyses, *act7* has severe defects in endosomal balance, which affect expression and PM location of all tested ABCBs and PIN2 with ABCB4 being the most disturbed, while PIN1 was only mildly concerned (Figures 3 and 4; Supplemental Figure 15). A more drastic perturbation of PM trafficking in *act7* is to be expected from the genetic loss of a structural actin cytoskeleton component, which should have more severe consequences on transporter trafficking than the loss of a bundling activity provided by TWD1.

Our data also provide a mechanistic explanation of why treatment of Arabidopsis roots with TIBA and NPA prevents the BFA-induced internalization of PIN1 and the trafficking of internalized PIN1 to the PM after BFA washouts (Geldner et al., 2001). The NPA concentration needed to reduce PIN1 cycling was 200  $\mu$ M (Geldner et al., 2001), which is in agreement with our *in vitro* NPA binding affinities found for TWD1. Our data now also provide a rationale for the NPA sensitivity of ABCB4-GFP localization in epidermal cells (Kubes et al., 2012).

**Figure 5.** (continued).

**(A)** *act7-4* like *twd1-1* shows a reduction in growth (upper panel; bar = 2 cm) and a significant disorientation of epidermal layers to the growth direction (twist angle, lower panel). Significant differences (unpaired *t* test with Welch's correction,  $P < 0.05$ ) between wild-type and mutant alleles are indicated with "a" and from solvent controls with "b" (means  $\pm$  SE;  $n = 4$  sets of 15 seedlings each).

**(B)** Analysis of planar root hair polarity in *act7* and *twd1* in the absence (upper panel) and presence of 1  $\mu$ M NPA (lower panel). Note apical (shootward) shifts in *act7-4* and *twd1-1* phenocopied by NPA treatments on the wild type. Color code of root hair positions is indexed from 0 (bottom) to 1 (top end of epidermal cells).

**(C)** Mutations in *twd1* and *act7* shift trichome development toward two-branched trichomes, phenocopying wild type treated with NPA. Shown is mean occurrence  $\pm$  SE of one- (red), di- (beige), tri- (green), and four-branched (blue) trichomes derived from  $n = 4$  independent sets of each 10 to 15 seedlings. Significant differences (unpaired *t* test with Welch's correction,  $P < 0.05$ ) are indicated with an "a."

**(D)** Destabilization and stabilization of actin by latrunculin B and jasplakinolide, respectively, block hook formation of etiolated seedlings to a similar degree as NPA. Significant differences (unpaired *t* test with Welch's correction,  $P < 0.05$ ) from solvent controls are indicated with an "a" and between wild-type and mutant alleles with a "b" (means  $\pm$  SE;  $n = 4$  sets of 20 seedlings each).

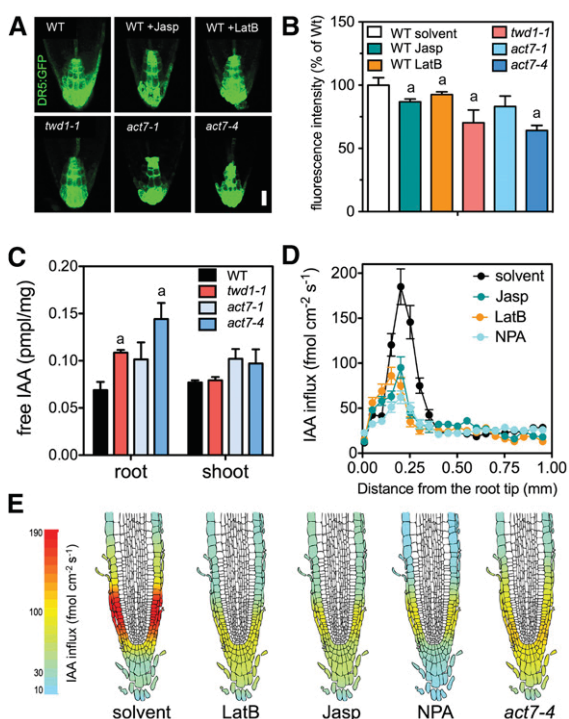


**Figure 6.** *twd1* and *act7* Show Overlapping Defects in Polar Auxin Transport.

(A) and (B) Root auxin responses visualized by the auxin-responsive element DR5:GFP are reduced in the *act7-4* and *twd1-1* columella [(B) quantification of (A)]. Bar = 20  $\mu\text{m}$ . (C) Free IAA is elevated in *act7-4* and *twd1-1* roots. (D) and (E) Influx profiles (D) and heat map presentation (E) of IAA influx along drug-treated (5  $\mu\text{M}$ ) wild-type and *act7-4* roots. Positive fluxes represent a net IAA influx. Significant differences (unpaired *t* test with Welch's correction,  $P < 0.05$ ) from wild-type solvent controls are indicated by "a." Mean  $\pm$  SE;  $n = 4$  sets of 20 [(A) to (C)] and 12 [(D) and (E)] seedlings each.

We further show that actin filament unbalancing (caused by pharmacological actin stabilization or destabilization) can block PAT to the same degree as NPA or loss of *ACT7* (Figure 6), resulting in similar phenotypic defects, exemplified here by hook opening (Figure 5). Therefore, our data provide further evidence that the actin cytoskeleton plays a direct role in PAT and that TWD1 functions as an integrating node of actin cytoskeleton organization/dynamics, vesicle trafficking, and PAT and mediates the action of NPA in these processes (Supplemental Figure 18). As a proof of concept, auxin-triggered physiology, such as root gravitropism, hypocotyl elongation, root hair positioning, and hook opening, but also actin filament organization and dynamics are largely not affected by NPA in *twd1*. Further indirect validation comes from the finding that *act7* and *twd1* mutants show overlapping developmental phenotypes that are dependent on local auxin gradients (Figure 6).

Our findings obviously also support the hypothesis that auxin regulates its own transport by unbundling actin filaments (Nick et al., 2009; Zhu and Geisler, 2015) and that auxin transport

inhibitors counteract this response through actin bundling, which is regulated by TWD1. However, it is important to recall that auxin transport inhibitors, such as NPA, are synthetic compounds for which the potential in planta counterparts are not known. Based on NPA displacement (Jacobs and Rubery, 1988), flavonols were originally discussed to work as plant-endogenous auxin transport inhibitors (Peer and Murphy, 2007). However, although flavonols efficiently disrupt TWD1-ABCB interaction (Bailly et al., 2008), based on our findings presented here (Supplemental Figure 1), flavonols seem unlikely to work via TWD1.

Although previous studies have established that ATI modulates actin bundling (Dhonukshe et al., 2008; Zhu and Geisler, 2015),

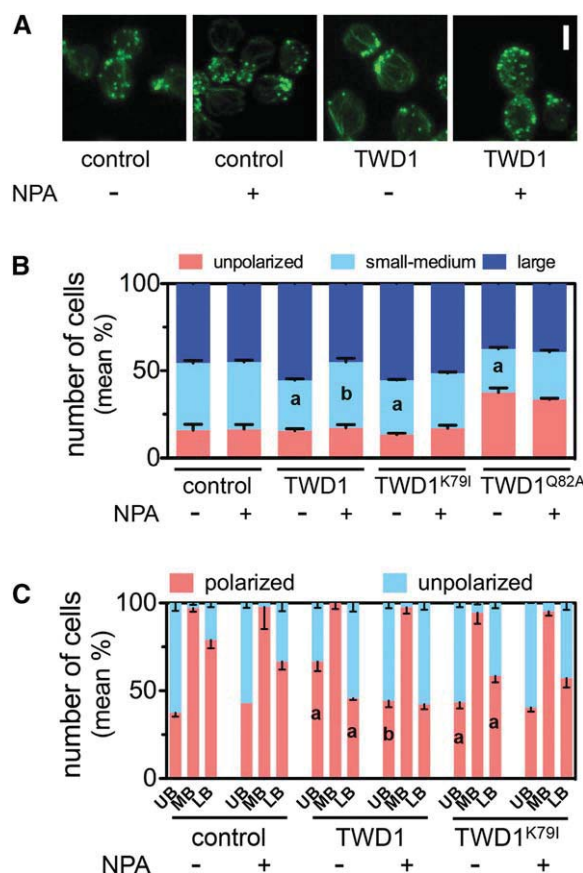


**Figure 7.** Expression of TWD1 Alters Yeast Budding and Actin Polarity and Confers NPA Sensitivity.

(A) Confocal images of wild-type yeast expressing TWD1 in the absence and presence of NPA (10  $\mu\text{M}$ ). Actin cables were stained in fixed yeast cells using phalloidin-Alexa Fluor488. Bar = 5  $\mu\text{m}$ .

(B) Bud size (unpolarized, small-to-medium buds, large buds) of wild-type yeast expressing TWD1 in the absence and presence of NPA (10  $\mu\text{M}$ ). Note NPA resistance of TWD1<sup>K79I</sup> and TWD1<sup>Q82A</sup> shown to not bind NPA (Supplemental Figure 4).

(C) Expression of TWD1 and TWD1<sup>K79I</sup> alters actin polarization, which is reverted by NPA in the wild type but not in TWD1<sup>K79I</sup>. Significant differences (unpaired *t* test with Welch's correction,  $P < 0.05$ ) between wild-type and mutant alleles are indicated by "a" and significant differences from solvent controls by "b" (mean  $\pm$  SE;  $n \geq 3$  independent transformants).

underlying mechanisms have not been investigated in detail. Here, we quantitatively resolved how NPA modifies various parameters of single AF dynamics (Table 2) and provide mechanistic insight into how TWD1 ultimately stimulates the overall actin bundling level in hypocotyls (Figure 2). Most importantly, our data revealed that NPA decreases AF dynamics/turnover (as indicated by increased AF lifetime and length) in a process involving both an increase of the elongation rate and a decrease of the severing frequency (Table 2). This effect likely accounts for the overall increase of actin bundling observed in NPA-treated hypocotyls (Supplemental Figure 18B) since NPA does not act by increasing the AF bundling frequency (Table 2). Remarkably, the various effects of NPA on single AF parameters were all abrogated in *twd1-1* mutants (Table 2), indicating that TWD1 is a key mediator of NPA action on AF dynamics. The finding that the *twd1-1* mutant exhibits defects in single AF parameters similar to those induced by NPA and resulted in a reduced turnover of AFs (Table 2) suggests a model where NPA inhibits this TWD1-mediated activity (axis 1 in Supplemental Figure 18B). Besides promoting AF destabilization, we found that TWD1 strikingly lowers the frequency of actin debundling (Table 2). This additional regulatory axis likely strengthens the increase of the overall actin bundling level in NPA-treated hypocotyls in a context where the actin dynamizing activity of TWD1 is blocked (Supplemental Figure 18B). NPA inhibits actin debundling apparently in a TWD1-independent manner; therefore, the regulatory components involved remain an open question.

Based on the outcome that TWD1 most likely does not autonomously bind to actin and directly control AF dynamics (Supplemental Figure 9), we propose third-party actin binding proteins as functional linker candidates (Thomas, 2012; Zhu and Geisler, 2015). The complex effect of TWD1 on AF organization and dynamics (i.e., a combined increase in actin dynamics and reduction in debundling) argues for the idea that TWD1 functionally interacts with two (or more) independent regulatory actin binding factors (Supplemental Figure 18B). According to this model, root-shoot-specific expression of TWD1-controlled regulatory actin binding proteins might account for the confusing opposite effects of auxin transport inhibitors on the overall actin cytoskeleton organization in roots and shoots (Rahman et al., 2007; Supplemental Figure 10). Importantly, like in hypocotyls, NPA action in roots requires TWD1, as indicated by the inability of NPA to increase the overall actin bundling level in *twd1-1* roots (Supplemental Figure 10). As expected, overall actin bundling in *act7-4* hypocotyls is NPA insensitive (Figure 2; Supplemental Figures 10A and 10B); however, this is apparently not the case in roots (Supplemental Figures 10C and 10D). Furthermore, unlike *act7-4* hypocotyls that reveal enhanced AF bundling compared with the wild type, root overall actin bundling is reduced (Supplemental Figures 10C and 10D). These findings argue for an involvement of root/shoot-specific actin binding proteins.

Potential TWD1-ACT7 linker candidates might belong to formin or villin families of actin binding proteins, which regulate actin organization and dynamics (Henty-Ridilla et al., 2013; Zhu and Geisler, 2015). For instance, Rice Morphology Determinant, a type II formin, was shown to link auxin-actin regulation by influencing cell growth (Li et al., 2014). Moreover, recently, downregulation of the three vegetative profilins, PRF1-3, was reported to result in a drastic dwarfed phenotype resembling *twd1* (Müssar et al.,

2015). Finally, Arabidopsis *vln2 vln3* and rice *vln2* mutants show a twisted disorientation of organs (van der Honing et al., 2012; Wu et al., 2015). For the rice *vln2* mutant, it was shown that developmental defects correlate with altered actin dynamics causing PIN2 delocalization and PAT defects (Wu et al., 2015). Future work should establish the exact nature of the actin binding proteins involved in TWD1-mediated regulation of polar auxin transport.

## METHODS

### NMR Spectroscopy

<sup>15</sup>N-labeled TWD1<sup>1-180</sup> from *Arabidopsis thaliana* was prepared as previously described (Kamphausen et al., 2002), except that the BL21 codon+RIL cells (Stratagene) were grown at 30°C in M9 minimal medium with <sup>15</sup>N-NH<sub>4</sub>Cl as the sole nitrogen source and harvested 3 h after induction with 0.5 mM IPTG. NMR samples contained 0.7 mM <sup>15</sup>N-labeled FKBP42<sup>1-180</sup> in 10 mM Na<sub>2</sub>HPO<sub>4</sub> buffer (5% D<sub>2</sub>O and 3% DMSO-d<sub>6</sub>, pH 7.0). For the chemical shift perturbation experiments, the TWD1<sup>1-180</sup> samples were supplemented with NPA (3.1 mM) or quercetin (0.7 mM), each administered in DMSO-d<sub>6</sub>. pH of all samples was controlled by a pH electrode before and after the NMR measurements and adjusted wherever needed.

NMR spectra were acquired at 25°C using a Bruker DRX500 spectrometer operating at 500.13 MHz proton resonance frequency and equipped with a 5-mm triple-resonance <sup>1</sup>H/<sup>13</sup>C/<sup>15</sup>N probe with gradient capability. Heteronuclear 2D <sup>1</sup>H/<sup>15</sup>N-HSQC spectra were collected with the carrier placed in the center of the spectrum on the water resonance, which was suppressed by applying a Watergate sequence. Quadrature detection in the indirectly detected dimension was obtained by the States-TPPI method. All NMR spectra were acquired and processed on Silicon Graphics computers using the program XWINNMR 3.5 (Bruker Bio-Spin). A 90° phase-shifted squared sine-bell function was used for apodization in all dimensions. Polynomial baseline correction was applied to the processed spectra in the directly detected <sup>1</sup>H dimension. The chemical shifts were referenced to external DSS in order to ensure consistency among all spectra. Spectra were analyzed with SPARKY 3 (University of California, San Francisco). Chemical shift differences in the amide proton ( $\Delta\delta_{1\text{HN}}$ ) and nitrogen ( $\Delta\delta_{15\text{N}}$ ) resonances of the free and complexed protein forms were combined for each residue using the expression  $[(\Delta\delta_{1\text{HN}})^2 + (\Delta\delta_{15\text{N}}/6.5)^2]^{1/2}$ .

### Quantum Chemical Modeling

A theoretical examination of the geometry, electronic structure, and electronic binding energies ( $\Delta E$ ) of the putative NPA binding pocket of TWD1 was performed using data from the crystal structure of the TWD1 FKBD (PDB accession code 2IF4). The orientations of the NPA molecule on the TWD1 binding surface were examined by molecular dynamic calculations using OPLS force fields. Next, the energetically most stable NPA-bound conformation in the TWD1 pocket (~500 atoms) was found by optimizing different geometries using Density Function Theory calculations including the Van der Waals correction D3 (DFT-D) with the bp86 functional and double-zeta polarized atomic basis set level [def-SV(P)]. The selection of the NPA cavity considered previous analyses of auxin molecules (Ferro et al., 2006), protein cavities (Rolo-Naranjo et al., 2010), and the NMR information. All calculations were performed with Gromacs (<http://www.gromacs.org/>) and Turbomole (<http://www.turbomole.com>).

Computational chemistry experiments were conducted to analyze the influence of the substitution mutants P37L, K39I, K79I, Q82A, and H125I. Their geometries were reoptimized at DFT-D level with bp86 and the D3 correction. The reoptimizations included both pocket-NPA pairs as well as NPA and pockets alone. Their binding forces were calculated according to the general equation  $\Delta E_{\text{cal}} = \Delta E_{\text{pocket}} - \text{NPA} - (\Delta E_{\text{pocket}} + \Delta E_{\text{NPA}})$  using the

accurate MGGA-based hybrid exchange correlation *functional* (TPSSH) and TZVP as basis set. The thermochemical analysis considered an average binding energy,  $\Delta P_{ave}$ , that consists of  $\Delta E_{ave} = \Delta E + \Delta E_{vdW} + \Delta E_{def}$  with the following parameters: effects of electronic binding energies ( $\Delta E$ ), Van der Waals forces ( $\Delta E_{vdW}$ ), and deformation energies of the protein ( $\Delta E_{def}$ ). The calculations solved the electronic problem of the interaction of NPA on the TWD1 protein surface pocket accurately and allowed calculations of average binding and further analysis of the potential surface and electronic density using the theory of deformed atoms in molecules (Fernández Rico et al., 2004).

$\Delta E$  values from QM analysis were approximately transformed into  $\Delta G$  values using the equation  $RT \ln(\Delta U)$  without taking into account the direct estimation of solvation ( $\Delta G_{sol}$ ) and entropic effects ( $T\Delta S$ ), which is given as follows:  $\Delta G = \Delta G_{sol} + \Delta U - T\Delta S$ .

### In Silico Substrate Docking to TWD1

One thousand poses for NPA and BA were generated using the PyMOL-embedded AutoDock Vina toolset (Seeliger and de Groot, 2010) as described (Bailey et al., 2011). To avoid any bias, the search space was first defined as the whole rigid TWD1 (PDB 2IF4; Granzin et al., 2006) structure with high exhaustiveness (Supplemental Figure 2). Calculations were further refined to the FKBD (FK506 binding domain; PDB 2F4E; Weiergräber et al., 2006) in flexible side-chain mode for the whole FKBP42<sup>34-180</sup> segment and resulted in 10 clusters with close conformations (Supplemental Figure 2).

### Affinity Purification of TWD1-CFP-Interacting Proteins and Mass Spectrometric Analysis

Coimmunoprecipitation analyses were performed in triplicate as described (Henrichs et al., 2012) except that bands of interest were size-selected by silver stain and manually cut out of the gel prior to trypsin digest. Liquid chromatography-MS/MS analyses were performed using an LTQ-Orbitrap XL-HTC-PAL system. MS/MS spectra were analyzed using the MASCOT server (version 2.2) searching the TAIR10 database (The Arabidopsis Information Resource). The MASCOT search parameters were as follows: set off the threshold at 0.05 in the ion score cutoff, peptide tolerance at 10 ppm, MS/MS tolerance at  $\pm 0.8$  D, peptide charge of 2+ or 3+, trypsin as enzyme allowing up to one missed cleavage, carboxymethylation on cysteines as a fixed modification and oxidation on methionine as a variable modification. Mascot-identified vector control proteins were subtracted manually from TWD1-CFP proteins, and proteins were sorted according to their appearance in triple experiments (identified counts) and listed according to their score (Supplemental Data Set 1). Mascot-identified proteins from three independent coimmunoprecipitation/mass spectrometry analyses were classified according to their putative biological process, their cellular components, and their molecular function using Blast2Go (www.blast2go.com).

### In Vitro TWD1-Actin Interaction Analyses

Binding of TWD1<sup>1-339</sup> and TWD1<sup>1-180</sup> (FKBD) proteins to rabbit actin filaments was assessed in high-speed cosedimentation assays. Briefly, increasing amounts (0.2 to 8  $\mu$ M) of TWD1<sup>1-180</sup> (Weiergräber et al., 2006) or TWD1<sup>1-339</sup> protein (Granzin et al., 2006) were incubated with pre-polymerized F-actin (4  $\mu$ M) under different pH conditions in the presence or absence of  $\text{CaCl}_2$  ( $\pm 303$   $\mu$ M) and centrifuged at 150,000g (Hoffmann et al., 2014a). The resulting pellet and supernatant fractions were analyzed by SDS-PAGE and Coomassie blue staining (or immunoblot analyses using anti-TWD1; Wang et al., 2013). The influence of TWD1 on AF polymerization kinetics was investigated in classical fluorimetric assays using pyrene-labeled actin filaments (3  $\mu$ M) with 12  $\mu$ M TWD1<sup>1-339</sup>  $\pm$  12  $\mu$ M NPA (Hoffmann et al., 2014a). The increase in pyrene fluorescence

accompanying actin polymerization was recorded over 1000 s using a PTI QM-4 QuantaMaster fluorimeter.

### Drug Binding Studies

Drug binding assays using Arabidopsis or yeast microsomes were performed as described elsewhere (Bailey et al., 2008). Four replicates of 20  $\mu$ g protein each were incubated with 10 nM radiolabeled NPA (ARC Inc.; 60 Ci/mmol) in the presence and absence of 10  $\mu$ M nonradiolabeled NPA. Reported values are the means of specific radiolabeled drug bound in the absence of cold drug (total) minus radiolabeled drug bound in the presence of cold drug (unspecific) from at least three independent experiments with four replicates each.

TWD1 was expressed in wild-type yeast strain JK93da (Hemenway and Heitman, 1996) from shuttle vector pRS314CUP:TWD1-Rluc (Bouchard et al., 2006). Point mutations in TWD1 (TWD1<sup>K39I</sup>, TWD1<sup>K79I</sup>, TWD1<sup>H125I</sup>, and TWD1<sup>Q82A</sup>) were introduced using the QuikChange XL site-directed mutagenesis kit (Stratagene).

NPA, TIBA, BUM, and BA binding of TWD1 was assayed by SPR on a Reichert SR7500DC instrument (Reichert Technologies). Ligand protein (TWD1<sup>1-339</sup> in 10 mM sodium acetate buffer pH 5) was immobilized on carboxymethyl dextran hydrogel sensor chips (CMD500m; XanTec Bioanalytics) to variable levels (15,000 to 19,000 uRIU) by thiol and amine coupling according to the manufacturers' instructions (GE Medical Systems; XanTec Bioanalytics). Analyte (NPA, BUM, TIBA, and BA) stock solutions (10 mM) and dilution series were prepared in ethanol and diluted into running buffer (10 mM HEPES, 150 mM NaCl, 10 mM  $\text{MgCl}_2$ , 10 mM KCl, 0.005% Tween 20, and 1% ethanol, pH 7.6) before addition of ethanol. For each experiment, at least three independent dilutions of analyte at the indicated concentrations were injected in duplicates, first over the immobilized ligand surface and subsequently over an L-cysteine (thiol coupling) or ethanolamine (amine coupling)-blocked reference channel at a flow speed of 20  $\mu$ L/min. No ligand regeneration was required due to fast and complete analyte dissociation. Baseline drift was minimal within experiments, and effects of mass transport were excluded in initial trials. Association and dissociation of the analytes were monitored for 120 s each. All experiments were performed at 25°C and included running buffer injections for double referencing. Double referencing and data analysis were performed using Scrubber2 (BioLogic Software) and Tracedrawer (Ridgeview Instruments) analysis software, respectively. Obtained sensograms were globally fitted with inclusion of a parameter correcting for local bulk index changes using a 1:1 Langmuir binding model (thiole coupling) or 1:2 surface heterogeneity model (amine coupling) for evaluation of kinetic parameters.  $k_a$ ,  $k_d$ ,  $K_{d(kin)}$ , and  $K_{d(eq)}$  were obtained from response data collected at near equilibrium toward the end of the injection and analyzed in Tracedrawer (Ridgeview Instruments) using the Affinity/EC50 tool.  $\Delta G^\circ$  was calculated using the formula  $\Delta G^\circ = RT \ln K_d$ . All experiments were repeated at least three times on independent sensor chips.

### Confocal Laser Scanning and Variable-Angle Epifluorescence Microscopy

For confocal laser scanning microscopy work, Leica TCS SP2, Leica TCS SP5, or Zeiss LSM780 equipment was used. Various confocal settings were set to record the emission of GFP (excitation 488 nm; emission 500 to 550 nm), CFP (excitation 458 nm; emission 468 to 500 nm), FM4-64, and LTR (excitation 543 nm; emission 580 to 640 nm). Whole-mount immunolocalizations in 5-dag Arabidopsis roots were performed as described (Friml et al., 2003). Images were acquired with the Leica confocal software 2.00 using identical settings for all samples. Antiserum concentrations were as follows: anti-TWD1 (1:500; Wang et al., 2013), anti-ARF1 (1:600; Agrisera; as08325), and CY3-conjugated anti-rabbit (1:600; sheep anti-rabbit IgG; Sigma-Aldrich; C2306). Polyclonal anti-PIN1 (1:500)

and anti-PIN2 (1:500) were raised in rabbits against amino acid epitopes 227-383 and 189-477, respectively as described by Abas et al. (2006) and Friml et al. (2003). Indicated peptides were expressed from vector pDEST17 and purified as N-terminally 6xHis-tagged versions as described by Friml et al. (2003). Short (2  $\mu$ M, 15 min) and long-term (4  $\mu$ M, 3 h) FM4-64 (ThermoFisher; T3166), LTR (ThermoFisher; L7528; 2  $\mu$ M, 60 min), BFA (Sigma-Aldrich; B7651; 25  $\mu$ M, 1 h) treatments were performed as described elsewhere (Wang et al., 2013).

For analysis of skewness in hypocotyls or roots of 5-dag GFP-fABD2 lines, we used Leica TCS SP5 and Zeiss LSM780 confocal microscopes, respectively. An approach similar to that of Higaki et al. (2010) generating maximum projections of static image stacks, applying Gaussian blur at 1.0 px radius and skeletonizing with the ThinLine function of the Kbi\_2d-filter package plug-in (<http://hasezawa.ib.k.u-tokyo.ac.jp/zip/Kbi/KbiFilter2d>) was employed. All actin image analyses were performed in the FIJI distribution of ImageJ 1.46a (<http://imagej.nih.gov/ij/>). Skewness parameters were obtained by the line features function of the package for the entire frame, comprising pictures of at least eight hypocotyls or roots. At least 60 cells were measured.

VAEM imaging of the cortical cytoplasm of epidermal cells was essentially as described (Hoffmann et al., 2014b). Illumination was achieved using a total internal reflection fluorescence illuminator mounted on an Axiovert 200 M microscope equipped with a 100 $\times$  1.46-NA TIRFM PlanApo objective (Zeiss). After focusing on the first visible actin filaments at the periphery of a cell, the angle of laser illumination was adjusted for maximal contrast and signal-to-noise ratio. We estimate the depth of focal plane at 0.5 to 1  $\mu$ m in VAEM mode. Illumination was from a 100-mW argon ion laser (attenuated to 5% power with neutral density filters and shuttered between consecutive exposures). The 488-nm laser line was filtered through a BP filter (N $^{\circ}$ 52; Zeiss) and GFP emission from the specimen captured with a 512  $\times$  512 electron-multiplying CCD camera (AxioCamHR3; Zeiss). Typical exposure times were around 600 ms.

For quantitative analyses, time-lapse series of around 100 images were collected at 2- to 3-s intervals and a table of elapsed time between each frame recorded. Cropped regions and subsets of the time-lapse images were converted to 7 frames per second QuickTime movies, without compression. To measure actin filament lengths, elongation rate, and severing frequency, actin filaments were tracked manually through the time-lapse stack of images as described in detail (Staiger et al., 2009). For filament lifetime, the definition of Henty et al. (2011) was used. Actin bundling and debundling frequencies were analyzed as described by Hoffmann et al. (2014a). At least 100 filaments from at least 20 different cells in 10 or more hypocotyls were selected. All single actin filament quantifications have been analyzed in double-blind analyses in order to avoid any bias.

### Auxin Transport

A platinum microelectrode was used to monitor IAA fluxes in Arabidopsis roots as described previously (Mancuso et al., 2005). For measurements, Wassilewskija (Ws) wild-type plants or *act7-4* were grown in hydroponic cultures and used at 5 dag. Differential current from an IAA-selective microelectrode was recorded in the absence and presence of 5  $\mu$ M NPA, jasplakinolide, or latrunculin B.

### In Planta Analysis of Auxin Contents and Responses

Endogenous free IAA was quantified from MeOH extracts of seedlings shoot and root segments using gas chromatography-mass spectrometry as described (Bouchard et al., 2006). Data are means of four independent lots of 30 to 50 seedlings each and equivalent to  $\sim$ 30 mg root and 60 mg shoot material, respectively.

Homozygous generations of Arabidopsis *act7-1/4*, *tdw1-1*, and *act7-4* *tdw1-1* seedlings (generated by crossing) were obtained by transformation with DR5<sub>rev</sub>:GFP (Ottenschläger et al., 2003). Seedlings were grown vertically for 5 dag and transferred overnight on 500 nM jasplakinolide or 20 nM latrunculin B plates and analyzed by confocal laser scanning microscopy.

### Plant Material and Phenotypic Analyses

The following Arabidopsis lines in ecotype Ws were used: *abcb1-1* (At2g36910), *abcb19-1* (At3g28860), and *abcb1-1 abcb19-1* (Noh et al., 2001); *tdw1-1* (At3g21640; Geisler et al., 2003); *act7-1* (At5g09810), *act7-4* (At5g09810), *act2-1* (At3g18780), *act8-2* (At1g49240), *act2-1 act7-1*, and *act7-4 act8-2* (Kandasamy et al., 2001; Gilliland et al., 2003); *TWD1:TWD1-CFP* (Wu et al., 2010); *ABCB1:ABCB1-GFP* and *ABCB19:ABCB19-GFP* (Mravec et al., 2008). *pin2/eir1-4* (At5g57090; Luschnig et al., 1998); *tdw1-3* (Geisler et al., 2003); *pin1-1* (At1g73590; Okada et al., 1991); *abcb19-3* (Lewis et al., 2007); *abcb1-100 abcb19-3* (Wu et al., 2010); *ABCB4:ABCB4-GFP* (At2g47000; Cho et al., 2007), 35S:HA-TWD1 (Geisler et al., 2003), *PIN1:PIN1-GFP* and *PIN2:PIN2-GFP* (Abas et al., 2006); GFP-fABD2 (Sheahan et al., 2004); and DR5:GFP (Ottenschläger et al., 2003) were all in the Columbia wild type (Col-0). *ABCB1:ABCB1-GFP*, *ABCB4:ABCB4-GFP*, *ABCB19:ABCB19-GFP*, *PIN1:PIN1-GFP*, *PIN2:PIN2-GFP*, *TWD1:TWD1-CFP*, *DR5<sub>rev</sub>:GFP*, and *35S:GFP-fABD2* transgenic lines were crossed into *act7-4* or *act7-6* (SALK\_131610; Kiefer et al. 2015), and isogenic, homozygous lines for the transgene in the F3 generations were used for further analyses. The same strategy was used for the *act7-4* *tdw1-1* crossing. In case nonisogenic lines were used for analyses (Figure 3), artifacts caused by ecotype mixes were excluded by immunolocalizations or employing isogenic controls (Supplemental Figure 13).

Seedlings were generally grown on vertical plates containing 0.5 Murashige and Skoog media, 1% sucrose, and 0.75% phytoagar in the dark or at 8 h (short day), 16 h (long day), or 24 h (constant) light per day. Developmental parameters, such as root gravitropism, hook opening, root hair positioning, trichome branching, and hypocotyl lengths, were quantified by microscopy as described (Masucci and Schiefelbein, 1994; Wang et al., 2013). Inhibitor concentrations were 400 nM jasplakinolide, 50 nM latrunculin B, and 5  $\mu$ M NPA. Root orientation of epidermal layers to the growth direction (twist angle) was quantified microscopically using agarose imprints as described (Wang et al., 2013). IAA-induced hypocotyl elongation was performed as described (Schenck et al., 2010). All experiments were performed at least in triplicate with 30 to 40 seedlings per each experiment.

### Yeast Polarity Analyses

TWD1 was expressed from shuttle vector pRS314CUP-TWD1 (Bouchard et al., 2006) in wild-type strain JK93da (Hemenway and Heitman, 1996). Yeast growth, cell polarity, and actin polarity were quantified in the wild type and KDY81.18c strain (Hemenway and Heitman, 1996) as described (Yu et al., 2011). To characterize the reorganization of actin cables during the cell cycle, cells were divided into three categories based on the size of daughter cells. These categories were unpolarized/unbudded cells, polarized to small-medium budded cells, and large budded cells. All data were derived from a minimum of three independent transformants.

### Data Analysis

Data were statistically analyzed using Prism 6.0 (GraphPad Software).

### Accession Numbers

Sequence data from this article can be found in the Arabidopsis Genome Initiative or GenBank/EMBL databases under the following accession numbers: ABCB1 (At2g36910), ABCB4 (At2g47000), ABCB19

(At3g28860), TWD1 (At3g21640), ACT1 (At5g09810), ACT2 (At3g18780), ACT7 (At5g09810), ACT8 (At1g49240), PIN1 (At1g73590), and PIN2 (At5g57090).

## Supplemental Data

**Supplemental Figure 1.** Superimposed  $^1\text{H}/^{15}\text{N}$ -HSQC spectra showing the backbone amide signals of TWD1 $^{1-180}$  in the presence of NPA and quercetin in comparison to the solvent.

**Supplemental Figure 2.** In silico docking and quantum chemical modeling of NPA and benzoic acid binding on TWD1.

**Supplemental Figure 3.** Structural analysis of wild-type and mutant versions of the TWD1 FKBD using quantum chemical modeling (DFT).

**Supplemental Figure 4.** NPA binding and regulatory effects of wild-type and mutated versions of TWD1 in yeast.

**Supplemental Figure 5.** Sensograms and representative fitted models of kinetic analyses and equilibrium analyses of surface plasmon resonance analyses of NPA, benzoic acid, BUM, and TIBA binding using thiol-immobilized TWD1 $^{1-339}$ .

**Supplemental Figure 6.** Root gravitropism and auxin-induced hypocotyl elongation of *tdw1-3* is less sensitive to NPA.

**Supplemental Figure 7.** Functional classification of TWD1-interacting proteins identified by coimmunoprecipitation followed by MS/MS analyses using TWD1:TWD1-CFP as a bait.

**Supplemental Figure 8.** TWD1 does not autonomously bind to mammalian actin filaments and affect actin polymerization.

**Supplemental Figure 9.** Confocal microscopy analyses of cortical actin bundling of hypocotyls and roots expressing GFP-fABD2 treated with 10  $\mu\text{M}$  NPA.

**Supplemental Figure 10.** Concentration dependency of NPA treatments causing bundling of cortical actin in hypocotyls.

**Supplemental Figure 11.** Hypocotyl length of *tdw1-1* and *act7-4* in the presence and absence of actin and microtubule stabilizing and destabilizing agents.

**Supplemental Figure 12.** *act7* single and double mutants reveal endosomal and vacuolar defects

**Supplemental Figure 13.** Expression and localization of PIN and ABCB-type auxin transporters are dependent on ACT7.

**Supplemental Figure 14.** Endosomal markers, Syp22, Syp61, and RabF2b, are delocalized in *act7-4* compared with the corresponding wild type.

**Supplemental Figure 15.** ABCB19 and PIN1 colocalize with endocytic marker FM4-64 after BFA treatment.

**Supplemental Figure 16.** Heat map presentation and influx profiles of IAA influx along wild-type, *tdw1-1*, and *act7-4* roots treated with 5  $\mu\text{M}$  latrunculin B, jasplakinolide, or the solvent.

**Supplemental Figure 17.** Analyses of FKBP action in yeast.

**Supplemental Figure 18.** Working model summarizing the function of FKBP42/TWD1 as an integrator of actin bundling and polar auxin transport.

**Supplemental Data Set 1.** TWD1 interacting proteins identified by coimmunoprecipitation followed by MS/MS analyses using TWD1-CFP as bait.

**Supplemental Movies 1 to 6.** Movies of time-lapse variable angle epifluorescence microscopy analyses of representative epidermal hypocotyl cells showing cortical actin labeled by fABD2-GFP of wild

type (Supplemental Movies 1 and 4), *tdw1-1* (Supplemental Movies 2 and 5) and *act7-4* (Supplemental Movies 3 and 6) in the absence (solvent controls; Supplemental Movies 1 to 3) and presence of NPA (1  $\mu\text{M}$ , 5 dag; Supplemental Movies 4 to 6).

## ACKNOWLEDGMENTS

We thank L. Charrier, V. Vincenzetti, F. Moreau, and P. DÜchting for outstanding technical assistance, N. Dankbar (XanTec) for SPR consultation, and E. Martinoia and J.P. Métraux for support and mentorship. The generosity of M. Hothorn is appreciated. This work was supported by grants from the European Social Fund (CZ.1.07/2.3.00/20.0043), the Czech Science Foundation GAČR (GA13-40637S) to J.F. and M.Z., the Ministry of Education, Youth, and Sports of the Czech Republic under the project CEITEC 2020 (LQ1601) to M.Z., the Ministry for Higher Education and Research of Luxembourg (REC-LOCM-20140703) to C.T., the Partial Funding Program for Short Stays Abroad of CONICET Argentina (to N.I.B.), Swiss National Funds, the Pool de Recherche of the University of Fribourg, and the Novartis Foundation (all to M.G.).

## AUTHOR CONTRIBUTIONS

M.G. and J.Z. designed research. J.Z., A.B., M.Z., V.S., M.D.D., P.G., J.O., B.A., N.I.B., E.A., C.H., and M.G. performed research. C.L., P.H., S.P., S.M., N.F., R.W.-S., Y.F., J.F., C.T., and M.G. analyzed data. M.L., M.W., M.M., and O.H.W. provided material. M.G., C.T., and V.S. wrote the manuscript.

## REFERENCES

- Abas, L., Benjamins, R., Malenica, N., Paciorek, T., Wiśniewska, J., Moulinier-Anzola, J.C., Sieberer, T., Friml, J., and Luschnig, C. (2006). Intracellular trafficking and proteolysis of the Arabidopsis auxin-efflux facilitator PIN2 are involved in root gravitropism. *Nat. Cell Biol.* **8**: 249–256. Erratum. *Nat. Cell Biol.* **8**: 424.
- Bailly, A., Sovero, V., Vincenzetti, V., Santelia, D., Bartnik, D., Koenig, B.W., Mancuso, S., Martinoia, E., and Geisler, M. (2008). Modulation of P-glycoproteins by auxin transport inhibitors is mediated by interaction with immunophilins. *J. Biol. Chem.* **283**: 21817–21826.
- Bailly, A., Wang, B., Zwiewka, M., Pollmann, S., Schenck, D., Lüthen, H., Schulz, A., Friml, J., and Geisler, M. (2014). Expression of TWISTED DWARF1 lacking its in-plane membrane anchor leads to increased cell elongation and hypermorphic growth. *Plant J.* **77**: 108–118.
- Bailly, A., Yang, H., Martinoia, E., Geisler, M., and Murphy, A.S. (2011). Plant lessons: exploring ABCB functionality through structural modeling. *Front. Plant Sci.* **2**: 108.
- Banasavadi-Siddegowda, Y.K., Mai, J., Fan, Y., Bhattacharya, S., Giovannucci, D.R., Sanchez, E.R., Fischer, G., and Wang, X. (2011). FKBP38 peptidylprolyl isomerase promotes the folding of cystic fibrosis transmembrane conductance regulator in the endoplasmic reticulum. *J. Biol. Chem.* **286**: 43071–43080.
- Barratt, E., Bingham, R.J., Warner, D.J., Loughton, C.A., Phillips, S.E., and Homans, S.W. (2005). Van der Waals interactions dominate ligand-protein association in a protein binding site occluded from solvent water. *J. Am. Chem. Soc.* **127**: 11827–11834.

- Blancaflor, E.B., Wang, Y.S., and Motes, C.M.** (2006). Organization and function of the actin cytoskeleton in developing root cells. *Int. Rev. Cytol.* **252**: 219–264.
- Bliilou, I., Xu, J., Wildwater, M., Willemsen, V., Paponov, I., Friml, J., Heidstra, R., Aida, M., Palme, K., and Scheres, B.** (2005). The PIN auxin efflux facilitator network controls growth and patterning in Arabidopsis roots. *Nature* **433**: 39–44.
- Bouchard, R., Bailly, A., Blakeslee, J.J., Oehring, S.C., Vincenzetti, V., Lee, O.R., Paponov, I., Palme, K., Mancuso, S., Murphy, A.S., Schulz, B., and Geisler, M.** (2006). Immunophilin-like TWISTED DWARF1 modulates auxin efflux activities of Arabidopsis P-glycoproteins. *J. Biol. Chem.* **281**: 30603–30612.
- Burgardt, N.I., Linnert, M., Weiwad, M., Geisler, M., and Lücke, C.** (2012). NMR assignments of the FKBP-type PPIase domain of FKBP42 from *Arabidopsis thaliana*. *Biomol. NMR Assign.* **6**: 185–188.
- Butler, J.H., Hu, S., Brady, S.R., Dixon, M.W., and Muday, G.K.** (1998). In vitro and in vivo evidence for actin association of the naphthylphthalamic acid-binding protein from zucchini hypocotyls. *Plant J.* **13**: 291–301.
- Casamayor, A., and Snyder, M.** (2002). Bud-site selection and cell polarity in budding yeast. *Curr. Opin. Microbiol.* **5**: 179–186.
- Cho, M., Lee, S.H., and Cho, H.T.** (2007). P-glycoprotein4 displays auxin efflux transporter-like action in Arabidopsis root hair cells and tobacco cells. *Plant Cell* **19**: 3930–3943.
- Cho, M., Lee, Z.W., and Cho, H.T.** (2012). ATP-binding cassette B4, an auxin-efflux transporter, stably associates with the plasma membrane and shows distinctive intracellular trafficking from that of PIN-FORMED proteins. *Plant Physiol.* **159**: 642–654.
- Cox, D.N., and Muday, G.K.** (1994). NPA binding activity is peripheral to the plasma membrane and is associated with the cytoskeleton. *Plant Cell* **6**: 1941–1953.
- Dhonukshe, P., et al.** (2008). Auxin transport inhibitors impair vesicle motility and actin cytoskeleton dynamics in diverse eukaryotes. *Proc. Natl. Acad. Sci. USA* **105**: 4489–4494.
- Dixon, M.W., Jacobson, J.A., Cady, C.T., and Muday, G.K.** (1996). Cytoplasmic orientation of the naphthylphthalamic acid-binding protein in zucchini plasma membrane vesicles. *Plant Physiol.* **112**: 421–432.
- Effendi, Y., Ferro, N., Labusch, C., Geisler, M., and Scherer, G.F.** (2015). Complementation of the embryo-lethal T-DNA insertion mutant of AUXIN-BINDING-PROTEIN 1 (ABP1) with abp1 point mutated versions reveals crosstalk of ABP1 and phytochromes. *J. Exp. Bot.* **66**: 403–418.
- Fernández Rico, J., López, R., Ema, I., and Ramírez, G.** (2004). Efficiency of the algorithms for the calculation of Slater molecular integrals in polyatomic molecules. *J. Comput. Chem.* **25**: 1987–1994.
- Friml, J., Benková, E., Mayer, U., Palme, K., and Muster, G.** (2003). Automated whole mount localisation techniques for plant seedlings. *Plant J.* **34**: 115–124.
- Geisler, M., Bailly, A., and Ivanchenko, M.** (2016). Master and servant: Regulation of auxin transporters by FKBP and cyclophilins. *Plant Sci.* **245**: 1–10.
- Geisler, M., Girin, M., Brandt, S., Vincenzetti, V., Plaza, S., Paris, N., Kobae, Y., Maeshima, M., Billion, K., Kolukisaoglu, U.H., Schulz, B., and Martinoia, E.** (2004). Arabidopsis immunophilin-like TWD1 functionally interacts with vacuolar ABC transporters. *Mol. Biol. Cell* **15**: 3393–3405.
- Geisler, M., and Murphy, A.S.** (2006). The ABC of auxin transport: the role of p-glycoproteins in plant development. *FEBS Lett.* **580**: 1094–1102.
- Geisler, M., Wang, B., and Zhu, J.** (2014). Auxin transport during root gravitropism: transporters and techniques. *Plant Biol. (Stuttg.)* **16** (suppl. 1): 50–57.
- Geisler, M., et al.** (2003). TWISTED DWARF1, a unique plasma membrane-anchored immunophilin-like protein, interacts with Arabidopsis multidrug resistance-like transporters AtPGP1 and AtPGP19. *Mol. Biol. Cell* **14**: 4238–4249.
- Geldner, N., Friml, J., Stierhof, Y.D., Jürgens, G., and Palme, K.** (2001). Auxin transport inhibitors block PIN1 cycling and vesicle trafficking. *Nature* **413**: 425–428.
- Gil, P., Dewey, E., Friml, J., Zhao, Y., Snowden, K.C., Putterill, J., Palme, K., Estelle, M., and Chory, J.** (2001). BIG: a calossin-like protein required for polar auxin transport in Arabidopsis. *Genes Dev.* **15**: 1985–1997.
- Gilliland, L.U., Pawloski, L.C., Kandasamy, M.K., and Meagher, R.B.** (2003). Arabidopsis actin gene ACT7 plays an essential role in germination and root growth. *Plant J.* **33**: 319–328.
- Granzin, J., Eckhoff, A., and Weiergräber, O.H.** (2006). Crystal structure of a multi-domain immunophilin from *Arabidopsis thaliana*: a paradigm for regulation of plant ABC transporters. *J. Mol. Biol.* **364**: 799–809.
- Grebe, M.** (2004). Ups and downs of tissue and planar polarity in plants. *BioEssays* **26**: 719–729.
- Hemenway, C.S., and Heitman, J.** (1996). Immunosuppressant target protein FKBP12 is required for P-glycoprotein function in yeast. *J. Biol. Chem.* **271**: 18527–18534.
- Henrichs, S., et al.** (2012). Regulation of ABCB1/PGP1-catalysed auxin transport by linker phosphorylation. *EMBO J.* **31**: 2965–2980.
- Henty, J.L., Bledsoe, S.W., Khurana, P., Meagher, R.B., Day, B., Blanchoin, L., and Staiger, C.J.** (2011). Arabidopsis actin depolymerizing factor4 modulates the stochastic dynamic behavior of actin filaments in the cortical array of epidermal cells. *Plant Cell* **23**: 3711–3726.
- Henty-Ridilla, J.L., Li, J., Blanchoin, L., and Staiger, C.J.** (2013). Actin dynamics in the cortical array of plant cells. *Curr. Opin. Plant Biol.* **16**: 678–687.
- Higaki, T., Kutsuna, N., Sano, T., Kondo, N., and Hasezawa, S.** (2010). Quantification and cluster analysis of actin cytoskeletal structures in plant cells: role of actin bundling in stomatal movement during diurnal cycles in Arabidopsis guard cells. *Plant J.* **61**: 156–165.
- Hoffmann, C., Moreau, F., Moes, M., Luthold, C., Dieterle, M., Goretta, E., Neumann, K., Steinmetz, A., and Thomas, C.** (2014a). Human muscle LIM protein dimerizes along the actin cytoskeleton and cross-links actin filaments. *Mol. Cell. Biol.* **34**: 3053–3065.
- Hoffmann, C., Moes, D., Dieterle, M., Neumann, K., Moreau, F., Tavares Furtado, A., Dumas, D., Steinmetz, A., and Thomas, C.** (2014b). Live cell imaging reveals actin-cytoskeleton-induced self-association of the actin-bundling protein WLIM1. *J. Cell Sci.* **127**: 583–598.
- Hülkamp, M., Miséra, S., and Jürgens, G.** (1994). Genetic dissection of trichome cell development in Arabidopsis. *Cell* **76**: 555–566.
- Holweg, C., Süßlin, C., and Nick, P.** (2004). Capturing in vivo dynamics of the actin cytoskeleton stimulated by auxin or light. *Plant Cell Physiol.* **45**: 855–863.
- Jacobs, M., and Rubery, P.H.** (1988). Naturally occurring auxin transport regulators. *Science* **241**: 346–349.
- Kamphausen, T., Fanghänel, J., Neumann, D., Schulz, B., and Rahfeld, J.U.** (2002). Characterization of *Arabidopsis thaliana* AtFKBP42 that is membrane-bound and interacts with Hsp90. *Plant J.* **32**: 263–276.
- Kandasamy, M.K., Gilliland, L.U., McKinney, E.C., and Meagher, R.B.** (2001). One plant actin isovariant, ACT7, is induced by auxin and required for normal callus formation. *Plant Cell* **13**: 1541–1554.
- Kandasamy, M.K., McKinney, E.C., and Meagher, R.B.** (2009). A single vegetative actin isovariant overexpressed under the control of multiple regulatory sequences is sufficient for normal Arabidopsis development. *Plant Cell* **21**: 701–718.

- Kania, U., Fendrych, M., and Friml, J.** (2014). Polar delivery in plants: commonalities and differences to animal epithelial cells. *Open Biol.* **4**: 140017.
- Kiefer, C.S., Claes, A.R., Nzayisenga, J.C., Pietra, S., Stanislas, T., Hüser, A., Ikeda, Y., and Grebe, M.** (2015). Arabidopsis AIP1-2 restricted by WER-mediated patterning modulates planar polarity. *Development* **142**: 151–161.
- Kim, J.Y., Henrichs, S., Bailly, A., Vincenzetti, V., Sovero, V., Mancuso, S., Pollmann, S., Kim, D., Geisler, M., and Nam, H.G.** (2010). Identification of an ABCB/P-glycoprotein-specific inhibitor of auxin transport by chemical genomics. *J. Biol. Chem.* **285**: 23309–23317.
- Kleine-Vehn, J., and Friml, J.** (2008). Polar targeting and endocytic recycling in auxin-dependent plant development. *Annu. Rev. Cell Dev. Biol.* **24**: 447–473.
- Kleine-Vehn, J., Dhonukshe, P., Swarup, R., Bennett, M., and Friml, J.** (2006). Subcellular trafficking of the Arabidopsis auxin influx carrier AUX1 uses a novel pathway distinct from PIN1. *Plant Cell* **18**: 3171–3181.
- Kubeš, M., et al.** (2012). The Arabidopsis concentration-dependent influx/efflux transporter ABCB4 regulates cellular auxin levels in the root epidermis. *Plant J.* **69**: 640–654.
- Lanza, M., et al.** (2012). Role of actin cytoskeleton in brassinosteroid signaling and in its integration with the auxin response in plants. *Dev. Cell* **22**: 1275–1285.
- Lewis, D.R., Miller, N.D., Splitt, B.L., Wu, G., and Spalding, E.P.** (2007). Separating the roles of acropetal and basipetal auxin transport on gravitropism with mutations in two Arabidopsis multidrug resistance-like ABC transporter genes. *Plant Cell* **19**: 1838–1850.
- Li, G., Liang, W., Zhang, X., Ren, H., Hu, J., Bennett, M.J., and Zhang, D.** (2014). Rice actin-binding protein RMD is a key link in the auxin-actin regulatory loop that controls cell growth. *Proc. Natl. Acad. Sci. USA* **111**: 10377–10382.
- Luschnig, C.** (2001). Auxin transport: why plants like to think BIG. *Curr. Biol.* **11**: R831–R833.
- Luschnig, C.** (2002). Auxin transport: ABC proteins join the club. *Trends Plant Sci.* **7**: 329–332.
- Luschnig, C., Gaxiola, R.A., Grisafi, P., and Fink, G.R.** (1998). EIR1, a root-specific protein involved in auxin transport, is required for gravitropism in *Arabidopsis thaliana*. *Genes Dev.* **12**: 2175–2187.
- Mancuso, S., Marras, A.M., Magnus, V., and Baluska, F.** (2005). Noninvasive and continuous recordings of auxin fluxes in intact root apex with a carbon nanotube-modified and self-referencing micro-electrode. *Anal. Biochem.* **341**: 344–351.
- Masucci, J.D., and Schiefelbein, J.W.** (1994). The rhd6 mutation of *Arabidopsis thaliana* alters root-hair initiation through an auxin- and ethylene-associated process. *Plant Physiol.* **106**: 1335–1346.
- Mravec, J., Kubes, M., Bielach, A., Gaykova, V., Petrusek, J., Skupa, P., Chand, S., Benkova, E., Zazimalova, E., and Friml, J.** (2008). Interaction of PIN and PGP transport mechanisms in auxin distribution-dependent development. *Development* **135**: 3345–3354.
- Muday, G.K.** (2000). Maintenance of asymmetric cellular localization of an auxin transport protein through interaction with the actin cytoskeleton. *J. Plant Growth Regul.* **19**: 385–396.
- Muday, G.K., and Murphy, A.S.** (2002). An emerging model of auxin transport regulation. *Plant Cell* **14**: 293–299.
- Murphy, A.S., Hoogner, K.R., Peer, W.A., and Taiz, L.** (2002). Identification, purification, and molecular cloning of N-1-naphthylphthalamic acid-binding plasma membrane-associated aminopeptidases from Arabidopsis. *Plant Physiol.* **128**: 935–950.
- Müssar, K.J., Kandasamy, M.K., McKinney, E.C., and Meagher, R.B.** (2015). Arabidopsis plants deficient in constitutive class profilins reveal independent and quantitative genetic effects. *BMC Plant Biol.* **15**: 177.
- Nagashima, A., et al.** (2008). Phytochromes and cryptochromes regulate the differential growth of Arabidopsis hypocotyls in both a PGP19-dependent and a PGP19-independent manner. *Plant J.* **53**: 516–529.
- Nick, P., Han, M.J., and An, G.** (2009). Auxin stimulates its own transport by shaping actin filaments. *Plant Physiol.* **151**: 155–167.
- Noh, B., Murphy, A.S., and Spalding, E.P.** (2001). Multidrug resistance-like genes of Arabidopsis required for auxin transport and auxin-mediated development. *Plant Cell* **13**: 2441–2454.
- Okada, K., Ueda, J., Komaki, M.K., Bell, C.J., and Shimura, Y.** (1991). Requirement of the auxin polar transport system in early stages of Arabidopsis floral bud formation. *Plant Cell* **3**: 677–684.
- Ottenschläger, I., Wolff, P., Wolverton, C., Bhalerao, R.P., Sandberg, G., Ishikawa, H., Evans, M., and Palme, K.** (2003). Gravity-regulated differential auxin transport from columella to lateral root cap cells. *Proc. Natl. Acad. Sci. USA* **100**: 2987–2991.
- Paciorek, T., Zazimalová, E., Ruthardt, N., Petrásek, J., Stierhof, Y.D., Kleine-Vehn, J., Morris, D.A., Emans, N., Jürgens, G., Geldner, N., and Friml, J.** (2005). Auxin inhibits endocytosis and promotes its own efflux from cells. *Nature* **435**: 1251–1256.
- Papuga, J., Hoffmann, C., Dieterle, M., Moes, D., Moreau, F., Tholl, S., Steinmetz, A., and Thomas, C.** (2010). Arabidopsis LIM proteins: a family of actin bundlers with distinct expression patterns and modes of regulation. *Plant Cell* **22**: 3034–3052.
- Peer, W.A., and Murphy, A.S.** (2007). Flavonoids and auxin transport: modulators or regulators? *Trends Plant Sci.* **12**: 556–563.
- Peer, W.A., Hosein, F.N., Bandyopadhyay, A., Makam, S.N., Otegui, M.S., Lee, G.J., Blakeslee, J.J., Cheng, Y., Titapiwatanakun, B., Yakubov, B., Bangari, B., and Murphy, A.S.** (2009). Mutation of the membrane-associated M1 protease APM1 results in distinct embryonic and seedling developmental defects in Arabidopsis. *Plant Cell* **21**: 1693–1721.
- Petrásek, J., Cerná, A., Schwarzerová, K., Elckner, M., Morris, D.A., and Zazimalová, E.** (2003). Do phototropins inhibit auxin efflux by impairing vesicle traffic? *Plant Physiol.* **131**: 254–263.
- Petrásek, J., et al.** (2006). PIN proteins perform a rate-limiting function in cellular auxin efflux. *Science* **312**: 914–918.
- Rahman, A., Bannigan, A., Sulaman, W., Pechter, P., Blancaflor, E.B., and Baskin, T.I.** (2007). Auxin, actin and growth of the *Arabidopsis thaliana* primary root. *Plant J.* **50**: 514–528.
- Rojas-Pierce, M., Titapiwatanakun, B., Sohn, E.J., Fang, F., Larive, C.K., Blakeslee, J., Cheng, Y., Cutler, S.R., Peer, W.A., Murphy, A.S., and Raikhel, N.V.** (2007). Arabidopsis P-glycoprotein19 participates in the inhibition of gravitropism by gravacin. *Chem. Biol.* **14**: 1366–1376. Erratum. *Chem. Biol.* **15**: 87.
- Rolo-Naranjo, A., Codorniu-Hernandez, E., and Ferro, N.** (2010). Quantum chemical associations ligand-residue: their role to predict flavonoid binding sites in proteins. *J. Chem. Inf. Model.* **50**: 924–933.
- Scheidt, H.A., Vogel, A., Eckhoff, A., Koenig, B.W., and Huster, D.** (2007). Solid-state NMR characterization of the putative membrane anchor of TWD1 from *Arabidopsis thaliana*. *Eur. Biophys. J.* **36**: 393–404.
- Schenck, D., Christian, M., Jones, A., and Lüthen, H.** (2010). Rapid auxin-induced cell expansion and gene expression: a four-decade-old question revisited. *Plant Physiol.* **152**: 1183–1185.
- Seeliger, D., and de Groot, B.L.** (2010). Ligand docking and binding site analysis with PyMOL and Autodock/Vina. *J. Comput. Aided Mol. Des.* **24**: 417–422.

- Sheahan, M.B., Staiger, C.J., Rose, R.J., and McCurdy, D.W.** (2004). A green fluorescent protein fusion to actin-binding domain 2 of Arabidopsis fimbrin highlights new features of a dynamic actin cytoskeleton in live plant cells. *Plant Physiol.* **136**: 3968–3978.
- Staiger, C.J., Sheahan, M.B., Khurana, P., Wang, X., McCurdy, D.W., and Blanchoin, L.** (2009). Actin filament dynamics are dominated by rapid growth and severing activity in the Arabidopsis cortical array. *J. Cell Biol.* **184**: 269–280.
- Szymanski, W.G., Zauber, H., Erban, A., Gorka, M., Wu, X.N., and Schulze, W.X.** (2015). Cytoskeletal components define protein location to membrane microdomains. *Mol. Cell. Proteomics* **14**: 2493–2509.
- Thomas, C.** (2012). Bundling actin filaments from membranes: some novel players. *Front. Plant Sci.* **3**: 188.
- Titapiwatanakun, B., et al.** (2009). ABCB19/PGP19 stabilises PIN1 in membrane microdomains in Arabidopsis. *Plant J.* **57**: 27–44.
- van der Honing, H.S., Kieft, H., Emons, A.M., and Ketelaar, T.** (2012). Arabidopsis VILLIN2 and VILLIN3 are required for the generation of thick actin filament bundles and for directional organ growth. *Plant Physiol.* **158**: 1426–1438.
- Vanneste, S., and Friml, J.** (2009). Auxin: a trigger for change in plant development. *Cell* **136**: 1005–1016.
- Wang, B., Bailly, A., Zwiewka, M., Henrichs, S., Azzarello, E., Mancuso, S., Maeshima, M., Friml, J., Schulz, A., and Geisler, M.** (2013). Arabidopsis TWISTED DWARF1 functionally interacts with auxin exporter ABCB1 on the root plasma membrane. *Plant Cell* **25**: 202–214.
- Weiergräber, O.H., Eckhoff, A., and Granzin, J.** (2006). Crystal structure of a plant immunophilin domain involved in regulation of MDR-type ABC transporters. *FEBS Lett.* **580**: 251–255.
- Wu, G., Otegui, M.S., and Spalding, E.P.** (2010). The ER-localized TWD1 immunophilin is necessary for localization of multidrug resistance-like proteins required for polar auxin transport in Arabidopsis roots. *Plant Cell* **22**: 3295–3304.
- Wu, S., et al.** (2015). VLN2 regulates plant architecture by affecting microfilament dynamics and polar auxin transport in rice. *Plant Cell* **27**: 2829–2845.
- Yu, J.H., Crevenna, A.H., Bettenbühl, M., Freisinger, T., and Wedlich-Söldner, R.** (2011). Cortical actin dynamics driven by formins and myosin V. *J. Cell Sci.* **124**: 1533–1541.
- Zádníková, P., et al.** (2010). Role of PIN-mediated auxin efflux in apical hook development of *Arabidopsis thaliana*. *Development* **137**: 607–617.
- Zhu, J., and Geisler, M.** (2015). Keeping it all together: auxin-actin crosstalk in plant development. *J. Exp. Bot.* **66**: 4983–4998.